NeuroImage 46 (2009) 692–707

Contents lists available at ScienceDirect

NeuroImage

journal homepage: www.elsevier.com/locate/ynimg

On the construction of a ground truth framework for evaluating voxel-based diffusion tensor MRI analysis methods

Wim Van Hecke [a,b,*], Jan Sijbers [a], Steve De Backer [a], Dirk Poot [a], Paul M. Parizel [b], Alexander Leemans [c,d]

[a] Visionlab (Department of Physics), University of Antwerp, Wilrijk (Antwerp), Belgium
[b] University Hospital Antwerp (Department of Radiology), University of Antwerp, Edegem (Antwerp), Belgium
[c] CUBRIC (School of Psychology), Cardiff University, Cardiff, UK
[d] Image Sciences Institute (Department of Radiology), University Medical Center Utrecht, Utrecht, The Netherlands

ARTICLE INFO

Article history:
Received 18 July 2008
Revised 9 February 2009
Accepted 17 February 2009
Available online 5 March 2009

Keywords:
Diffusion tensor imaging
Voxel-based analysis
Simulated data
Coregistration
Atlas construction

ABSTRACT

Although many studies are starting to use voxel-based analysis (VBA) methods to compare diffusion tensor images between healthy and diseased subjects, it has been demonstrated that VBA results depend heavily on parameter settings and implementation strategies, such as the applied coregistration technique, smoothing kernel width, statistical analysis, etc. In order to investigate the effect of different parameter settings and implementations on the accuracy and precision of the VBA results quantitatively, ground truth knowledge regarding the underlying microstructural alterations is required. To address the lack of such a gold standard, simulated diffusion tensor data sets are developed, which can model an array of anomalies in the diffusion properties of a predefined location. These data sets can be employed to evaluate the numerous parameters that characterize the pipeline of a VBA algorithm and to compare the accuracy, precision, and reproducibility of different post-processing approaches quantitatively. We are convinced that the use of these simulated data sets can improve the understanding of how different diffusion tensor image post-processing techniques affect the outcome of VBA. In turn, this may possibly lead to a more standardized and reliable evaluation of diffusion tensor data sets of large study groups with a wide range of white matter altering pathologies. The simulated DTI data sets will be made available online (http://www.dti.ua.ac.be).

Introduction

Diffusion tensor magnetic resonance imaging (DTI) is a unique medical imaging modality that provides estimates of the directionality as well as the magnitude of water diffusion (Basser et al., 1994). Recently, several studies demonstrated that diffusion tensor (DT) derived metrics have the potential for revealing subtle white matter (WM) differences in a wide range of pathologies and neuropsychiatric conditions (Rovaris and Filippi, 2007; Bozzali and Cherubini, 2007; Cherubini et al., 2007). In this context, fractional anisotropy (FA), which is a normalized measure of the degree of diffusion anisotropy, and mean diffusivity (MD), i.e. the average amount of diffusion, are generally examined and have been related to the integrity of WM bundles (Beaulieu, 2002). However, to increase the utility of DTI in both research and the daily clinical routine, large scale, quantitative DTI studies of different pathologies are required to further investigate the effect of microstructural WM alterations – induced by a given disorder – on the spatial location, the extent, and the magnitude of diffusion related DTI changes.

In order to compare diffusion properties across subjects quantitatively, many studies perform a region of interest (ROI) analysis, in which these ROIs are marked on locations that have been associated with abnormalities for a given pathology (Molko et al., 2001; Abe et al., 2002; Wang et al., 2003; Kubicki et al., 2002; Kumra et al., 2004; Kubicki et al., 2003; Westerhausen et al., 2003; Snook et al., 2005, 2007). Although this approach is straightforward and has gained its merits in earlier studies, several drawbacks prevent it from being the analysis tool of choice for large scale, standardized DTI studies. These drawbacks include the labor intensity of the method, a restricted reproducibility due to the observer dependent ROI placement, difficulties to outline the complex 3D WM architecture by 2D ROIs, and the dependence of the results on the a priori hypothesis that is made regarding the spatial location and extent of the differences. Combined with the subject group and disease heterogeneity, including confounding factors such as age, sex, handedness, disease state, etc., these aforementioned limitations can explain the inconsistency of the published diffusion values that were derived by the ROI analysis, as for example in the study of patients with Multiple Sclerosis (MS) (Hasan et al., 2005; Ciccarelli et al., 2003; Cercignani et al., 2002;

* Corresponding author. Vision lab, Department of Physics University of Antwerp Universiteitsplein 1, N 1.18, B-2610 Antwerpen, Belgium. Fax: +32 0 3 820 22 45.
E-mail address: k.wim.vanhecke@ua.ac.be (W. Van Hecke).

1053-8119/$ – see front matter © 2009 Elsevier Inc. All rights reserved.
doi:10.1016/j.neuroimage.2009.02.032

Pfefferbaum et al., 2000; Bammer et al., 2000; Griffin et al., 2001; Ge et al., 2004; Yu et al., 2007).

To mitigate the limitations of the ROI approach, an automated voxel-based analysis (VBA) is increasingly being used to study DT alterations for many diseases. In VBA, all data sets are spatially normalized to a certain template, whereafter a voxel-by-voxel statistical comparison between the control subjects and the patients is performed (Ashburner and Friston, 2000). In this way, the whole brain is tested for control-patient differences without any a priori hypothesis of the expected spatial location of the abnormalities to be made. Furthermore, although the VBA approach is computationally more intensive, it is far less laborious compared to the ROI method. In addition, the user-dependency of the ROI approach is replaced by a parameter-dependency in VBA, making the subsequent quantitative analysis more reproducible and standardized. However, for example in the published DTI studies of patients with schizophrenia, there is no general correspondence between the findings (Agartz et al., 2001; Foong et al., 2002; Ardekani et al., 2003; Burns et al., 2003; Szeszko et al., 2005; Kubicki et al., 2005; Ardekani et al., 2005; Buchsbaum et al., 2006; Jones et al., 2007; Douaud et al., 2007; Seok et al., 2007; Karlsgodt et al., 2007; Kyriakopoulos et al., 2007; White et al., 2007). Significant FA differences between healthy subjects and schizophrenia patients were reported in a large range of white matter structures, such as for example the cerebellar peduncle (Seok et al., 2007; Kyriakopoulos et al., 2007), cortico-spinal tracts with schizophrenia (Douaud et al., 2007), internal capsule with schizophrenia (Kubicki et al., 2005; Buchsbaum et al., 2006), genu of the corpus callosum with schizophrenia (Ardekani et al., 2003; Douaud et al., 2007), splenium of the corpus callosum with schizophrenia (Ardekani et al., 2003; Douaud et al., 2007; Kyriakopoulos et al., 2007), forceps major with schizophrenia (Agartz et al., 2001; Kyriakopoulos et al., 2007), body of the corpus callosum with schizophrenia (Douaud et al., 2007), superior longitudinal fasciculus with schizophrenia (Kubicki et al., 2005; Buchsbaum et al., 2006; Seok et al., 2007; Kyriakopoulos et al., 2007), and cingulum (Kubicki et al., 2005; Seok et al., 2007). The subject group and disease heterogeneity across the different studies, including confounding factors such as age, sex, handedness, disease state, etc., can partially explain these observed discrepancies. However, methodological differences in implementation of VBA are possibly even more decisive for explaining the variances in the VBA results of different studies.

Jones et al. (2005, 2007) and Zhang et al. (2007) demonstrated that different VBA results were obtained when different coregistration techniques, smoothing kernels, statistics, etc. were implemented during the VBA analysis of the same subject group. Since the location and extent of the underlying microstructural degradation was not known a priori in these studies, quantitative information regarding the accuracy, precision, or reliability of the obtained VBA results cannot be provided. As such, these studies clearly demonstrate the need for a gold standard for validating different post-processing methods and their relative merits.

To address the lack of ground truth knowledge regarding the underlying microstructural alterations, in this work, simulated DTI data sets are developed, which allows for modeling of anomalies in the diffusion properties of a predefined location and in a predefined number of voxels. In this context, an important requisite for the validity of the simulated DTI data sets is to model the induced pathology by simulating these diffusion properties accurately and realistically (Leemans et al., 2005b). To the best of our knowledge, this is the first framework that allows for constructing simulated DTI data sets with ground truth information of pathology. These simulated DTI data sets can be used to investigate the reliability, accuracy, and precision of a VBA or ROI analysis.

In addition, the effect of the different parameters and post-processing steps that are involved in the pipeline of a VBA analysis can be examined, which could lead to a more reliable, standardized, and consistent post-processing of DT images for studying different pathologies.

Methods

Ground truth framework

In this work, simulated DTI data sets are constructed that contain a ground truth pathology with a predefined location, extent, and level of tissue degradation. In Fig. 1, a general overview of the construction of these simulated DTI data sets is presented and can be summarized as follows:

(a) H healthy subject and P pathology DTI data sets are acquired.
(b) The N (where$N = H + P$) DTI data sets are transformed to the Montreal Neurological Institute (MNI) space with an affine transformation.
(c) Based on the N images in MNI space, a population specific atlas is constructed for the H healthy subjects.
(d) The atlas forms the fundamental data set of the ground truth method and is replicated N times.
(e) In P atlases, the diffusion properties are altered to introduce a pathology in certain voxels.
(f) The diffusion properties are modified to include inter-subject variability.
(g) All data sets are transformed to their native space.
(h) Noise is added to the data sets.

In the following sections, these steps are described in more detail.

Native images

The ground truth method is based on the acquisition of H diffusion tensor data sets of healthy subjects and P diffusion tensor data sets of subjects with a certain pathology (Fig. 1a). These native healthy subject and pathology data sets will be referred to as O_h (with $h = 1, \ldots, H$) and O_p (with $p = H+1, \ldots, H+P$), respectively. In general, the subject data of the entire group will be denoted as O_i ($i = 1, \ldots, N$), with N the total number of subjects: $N = H + P$. When not explicitly specified that the diffusion weighted (DW) images or the diffusion tensor components are used, the subject data O_i reflect both the DW images and the diffusion tensor components. With DW images, we refer to the set of 60 diffusion images, one for each gradient direction.

Atlas construction

A first step in the framework of the simulated data sets is the construction of a population specific DTI atlas based on the N native images (Figs. 1b and c). This process involves different steps, as described in Van Hecke et al. (2008), and can be summarized as follows (see also Fig. 1i):

- From the EPI MNI template, a custom FA based template was constructed as described in Jones et al. (2002). All subjects data Oi (with $i = 1, \ldots, N$) are spatially normalized to this custom FA MNI template with an affine transformation of the FA images using MIRIT (Multimodality Image Registration using Information Theory), incorporating the preservation of principal direction (PPD) tensor reorientation strategy (Alexander et al., 2001; Leemans et al., 2005a; Maes et al., 1997). The transformed images will be referred to as I_h and I_p, or more generally as I_i (see Fig. 1b).
- Non-affine deformation fields Tji of data set Ii to data set Ij ($i,j = 1, \ldots, N$, $i \neq j$) are calculated for each image of the subject group (see Fig. 1i). For the non-affine image alignment procedure, a coregistration algorithm based on a viscous fluid model and mutual information is used, which has been optimized to incorporate all DT information (Van Hecke et al., 2007; D'Agostino et al., 2003).
- The deformation fields Tji (with $j = 1, \ldots, N$ and $j \neq i$) are averaged for each image I_j $\left(T_i = \frac{1}{N-1}\sum_j T_{ji}\right)$. The deformation fields T_i characterize the anatomical variation between image I_i and all other data sets of the subject group.

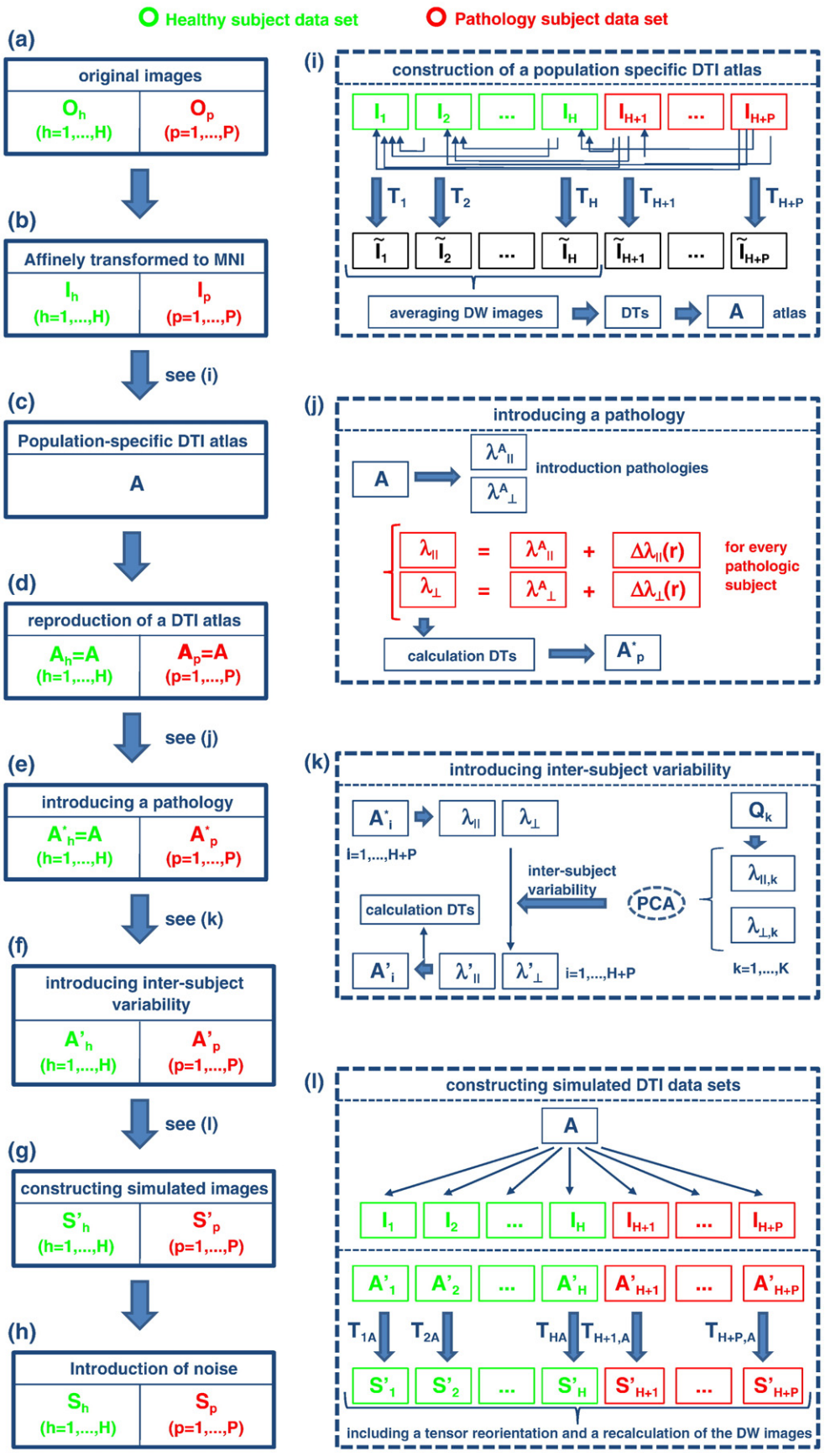

Fig. 1. A schematic overview of the ground truth method is presented. On the left, the main steps of this method are displayed in (a)–(h), including the construction of a population-based atlas, the introduction of a pathology, inter-subject variability, and noise, and the deformation of the images to native space. More specific information about the different steps is provided in (i)–(p). All data sets O_i, I_i, A_i, A_{*i}, A, S_i and S_i contain both the DW images and the diffusion tensor components. The healthy subject data sets are coloured in green, whereas the pathology subject data sets are coloured in red.

- The deformation fields *Ti* are applied to all DW images of data sets *Ii*. After estimating the diffusion tensor from the transformed DW images, the PPD reorientation strategy is applied to obtain the correct diffusion tensors (Alexander et al., 2001). From these reoriented diffusion tensors, the DW images DW_k that correspond to this new space are recalculated using the following equation:

$$DW_k = DW_0 \cdot e^{-b_k D}, \tag{1}$$

with DW_0 the non-diffusion weighted image, b_k the diffusion gradient information along direction k, and D the diffusion tensor. At this stage, if D is known, or modeled with a predefined pathology, then DW_k can be recalculated using this diffusion equation (Jones and Basser, 2004). This back projection approach to simulate DW images from a predefined tensor is explained in detail in Jones and Basser (2004). In doing so, the DW images can be averaged appropriately, since the corresponding DW images of different subjects are situated in the same space. The resulting DTI data sets in atlas space are referred to as $\tilde{I}_i$ ($\tilde{I}_i = T_i(I_i)$) (see Fig. 1i). More specifically, the healthy and pathology subject data sets in atlas space are referred to as $\tilde{I}_h$ and $\tilde{I}_p$, respectively.

- The atlas A is constructed by a voxel-wise averaging of the DW images of the *H*healthy data sets in atlas space$\tilde{I}h$ followed by a recalculation of the diffusion tensors (see Fig. 1i). Note that the application of an iterative estimation procedure to construct the population-based DTI atlas A did not significantly improve the accuracy of the diffusion tensor atlas (Van Hecke et al., 2008).

Notice that a healthy subject atlas is constructed, since only the H data sets of the healthy subjects in atlas space $\tilde{I}_h$ are averaged to compute this atlas. As such, the diffusion properties of the pathology subjects are not included in the atlas. However, notice that the data sets of these P pathology subjects are still used during the atlas construction to calculate the deformation fields T_i ($i = 1, \ldots, N$). Hence, an atlas is constructed that represents a structural averaged image of the whole subject group, including the pathology subjects, but only containing diffusion properties of the healthy subjects. This population specific atlas is regarded as the fundamental image in our ground truth VBA methodology and will be referred to as A (see Fig. 1c). All simulated data sets will be constructed from this atlas A. To this end, A is replicated N times, resulting in N times the same atlas data set $A_i = A$ (see Fig. 1d).

Introducing pathology

In DTI, a WM pathology can present itself generally in two different ways: as a more global morphological anomaly on the one hand and as local changes in diffusion properties on the other hand. In the former case, WM structures are altered due to the presence of brain atrophy, the growth of a tumor, or changes in ventricle size, etc. Commonly, these anomalies can also be detected on conventional MR images. The resulting WM deviations can be visualized with diffusion tensor tractography, a virtual reconstruction of the WM fiber pathways (Basser et al., 2000; Lee et al., 2005; Catani, 2006).

Since the changes in local diffusion properties can be related to changes in organization of the underlying microstructure, they can provide sensitive markers of brain WM integrity, which is not always available with conventional MR examinations. These diffusion parameters can quantify the underlying mechanisms leading to neurological dysfunction in WM disorders, such as demyelination or axonal breakdown to a certain extent (Beaulieu, 2002). Note, however, that – although the diffusion properties can be related to WM breakdown – the specific relationship between WM changes and pathology is still poorly understood. Despite this limitation, most DTI studies of pathologies examine these diffusion discrepancies using an ROI or VBA method. Therefore, in this framework, these diffusion alterations, which can be associated with a neurologic disorder, are introduced in different WM structures of the ground truth data sets, which are subsequently regarded as belonging to the pathology group.

Although further studies are needed, recent work suggests that demyelination and axonal degeneration cause an increase of the average of the second and third eigenvalues (the transverse diffusivity, $\lambda_\perp^A$) and a decrease of the first eigenvalue (the longitudinal diffusivity, $\lambda_\parallel^A$), respectively (Song et al., 2002, 2003, 2005; Budde et al., 2007; Schwartz et al., 2005; Harsan et al., 2006). In our work, these measures are therefore used to simulate axonal damage, myelin injury, or a combination of both in the DTI data sets. Notice that, in addition to the location and extent of the pathology, the level of tissue degradation, as reflected by the diffusion properties, can also be controlled in the simulated pathology data sets.

For each pathology data set, the eigenvalue alterations are introduced in the longitudinal $\lambda_\parallel^A$ and transverse $\lambda_\perp^A$ eigenvalue images of the atlas data sets A_p ($p = 1, \ldots, P$), which are subsequently regarded as the pathology group, resulting in the eigenvalue images $\lambda_\parallel$ and $\lambda_\perp$ (see Figs. 1e and j):

$$\begin{aligned} \lambda_\parallel(\mathbf{r}) &= \lambda_\parallel^A(\mathbf{r}) + \Delta\lambda_\parallel(\mathbf{r}) \\ \lambda_\perp(\mathbf{r}) &= \lambda_\perp^A(\mathbf{r}) + \Delta\lambda_\perp(\mathbf{r}) \end{aligned}. \tag{2}$$

The magnitude of the microstructural breakdown that is simulated in the longitudinal and transverse eigenvalue images is defined as $\Delta\lambda_\parallel(\mathbf{r})$ and $\Delta\lambda_\perp(\mathbf{r})$, respectively, where $\mathbf{r}$ describes the location and size of the different voxel clusters in which a pathology is introduced for the longitudinal and transverse eigenvalue images. Note that $\Delta\lambda_\parallel(\mathbf{r})$ and $\Delta\lambda_\perp(\mathbf{r})$ can be defined for each data set separately. The microstructural breakdown, represented by $\Delta\lambda_\parallel(\mathbf{r})$ and $\Delta\lambda_\perp(\mathbf{r})$, is introduced as a percentage change of the original values $\lambda_\parallel^A$ and $\lambda_\perp^A$. Note that $\Delta\lambda_\parallel(\mathbf{r})$ and $\Delta\lambda_\perp(\mathbf{r})$ can be modeled more specifically to constrain changes in FA and MD. For example, a FA decrease can be simulated while keeping the MD constant.

Since the purpose is to introduce eigenvalue alterations, and not to change the main direction of diffusion, care has to be taken that the transverse diffusivity does not become larger than the longitudinal diffusivity. The altered eigenvalue images $\lambda_\parallel$ and $\lambda_\perp$ are subsequently used to redefine the new diffusion tensors. Note that in this model of introducing pathology, the diffusion eigenvectors are not modified and that radial diffusion symmetry is assumed, i.e., the second and third eigenvalues are changed in the same way. After the modification of the diffusion tensor, the DW images are recalculated. The resulting data sets A_p^* represent the atlas images with an additional simulated pathology in certain voxels (see Fig. 1e). The data sets that are regarded as the simulated healthy subject images are not altered during this step of the processing pipeline: $A_h^* = A_h$.

Introducing inter-subject variability

Even if data sets of different healthy subjects are acquired in the same scanner and with the same acquisition parameters, a significant inter-subject variance can be observed in these images. Many variables, such as age, sex, handedness, etc. of the subjects are known to contribute to this variability in the DT properties (Huster et al., 2009; Hsu et al., 2008). Therefore, most VBA and ROI studies circumvent these sources of variation by a careful selection of the subject groups. However, due to the inherent anatomical and physiological variability across subjects, the inter-subject variance is still present in the DTI data sets. In order to create more realistic DT images in our ground truth framework, this inter-subject variability should be integrated to both healthy A_h^* ($h = 1, \ldots, H$) and pathology A_p^* ($p = 1, \ldots, P$) data sets.

Analogously to the WM pathology, the inter-subject variability can present itself as a morphological WM variability or as variances of the diffusion properties. Examples of the former are the shape variance of the corpus callosum and the difference in the frontal WM architecture across healthy subjects. The latter source of inter-subject variability is more subtle, but will affect the statistics when different diffusion

properties are compared between subject groups. Simulation of this type of inter-subject variance was obtained using a principal component analysis (PCA) on the longitudinal and the transverse eigenvalue images, since they contain all the information regarding the local diffusion properties. Variances in the local directional diffusion information, which can be considered as morphological WM variabilities, will be accounted for in a later step of the ground truth method. New longitudinal and transverse eigenvalue samples are produced from an estimated distribution, as explained as follows (see Fig. 1k):

- First, the DT atlas A is masked by thresholding the FA map. An FA threshold of 0.2 was used to suppress areas consisting of cerebrospinal fluid (CSF) and deep gray matter (GM) in the analysis (Smith et al., 2006).
- K healthy subject DTI data sets are acquired to estimate the inter-subject variance of the diffusion properties. These K data sets are coregistered non-affinely to the DTI atlas A, resulting in the data sets Q_k ($k=1, \ldots, K$) (see Fig. 1k).
- Subsequently, a vector is constructed as a concatenation of the masked longitudinal and transverse eigenvalue images of all data sets Qk ($k=1, \ldots, K$). Hence, a $2V$-dimensional vector is obtained for each data set Q_k, with V the number of voxels included in the mask.
- Let M represent a $K\times 2V$ matrix, containing all the data. This data was made zero-mean by subtracting the mean 2V-vector for every row. In other words, the mean longitudinal eigenvalue image is subtracted from the K longitudinal eigenvalue images. The same is done for the transverse eigenvalue images. Since $K \ll 2V$, the K-dimensional subspace is used to generate new samples. For this, the eigenvalue decomposition $MM^T = E\Lambda E^T$ is calculated, with E an orthogonal matrix containing the eigenvectors, and Λ a diagonal matrix containing the eigenvalues of a $(K\times K)$ matrix.
- A new random sample R is generated as a $K\times 1$ vector which is defined as zero-mean, unit variance, Gaussian distributed random variables. This sample is projected to the $2V$-dimensional space using $\frac{1}{\sqrt{K}} M^T ER$
- Finally, the mean vector is added to these samples, which are then distributed according to the K original ones.

In this way, inter-subject variability is added to the longitudinal and transverse eigenvalues of both the healthy and pathology data sets, followed by a recalculation of the diffusion tensors and the DW images. The resulting healthy and subject pathology data sets are referred to as A'_h and A'_p, respectively (Table1).

Constructing the simulated data sets

As described in the paragraphs 3 and 4, the local diffusion properties were altered to include a pathology and inter-subject variability in the simulated DTI data sets. However, the resulting DT images are still situated in the atlas space of image A.

Realistic, simulated DTI data sets of different individuals are created by generating non-affine deformation fields that warp the data sets A'_h and A'_p to their respective subject spaces. These transformations are obtained by calculating the non-affine deformation fields between the atlas A and the native data sets I_i in the affine MNI space (see Fig. 1l). Since realistic deformation fields, derived from the coregistration of A to different healthy subjects I_h, are used to transform the images A'_h, the inter-subject variability of the WM structures in native space is also taken into account appropriately. Structural WM pathologies and inter-subject variability of the WM structures are also included in the transformed images A'_p, since P deformation fields are obtained from the coregistration of A to the DTI data sets of the pathology subjects I_p.

In order to increase the accuracy of the inter-subject warps and to decrease the dependency of the spatial information of the simulated data sets on a single coregistration algorithm, three different image normalization methods are combined to compute a more general deformation field:

1. The aforementioned viscous fluid model, including all DT information during the image alignment, is used to obtain the deformation fields TiA^1 between the atlas A and the native data sets Ii.
2. The deformation fields T^2_{iA} are computed using a coregistration approach that is based on free-form deformations and B-splines, which is included in software packages as IRTK (Image Registration Toolkit) and FSL (FMRIB Software Library — www.fmrib.ox.ac.uk/fsl) (Rueckert et al., 1999).
3. The deformation fields TiA^3 are obtained by a linear combination of $(7\times 8\times 7)$ basis functions as is included in the SPM package (Ashburner and Friston, 1999).

Note that T^1_{iA} is obtained by incorporating all DT information during the coregistration, whereas FA maps are employed to obtain both T^2_{iA} and T^3_{iA}. The total non-affine transformation of the atlas A to each native images I_i is calculated as the average of the three deformation fields:

$$T_{iA} = \frac{1}{3}\sum_{j=1}^{3} T^j_{iA}$$

These deformation fields are applied to the DW images of the data sets A'_h and A'_p, followed by a calculation of the diffusion tensors and a tensor reorientation. The accordingly obtained simulated DTI data sets will be referred to as $S'_h = T_{hA}(A'_h)$ ($h=1, \ldots, H$) and $S'_p = T_{pA}(A'_p)$ ($p=1, \ldots, P$), or as S_i ($i=1, \ldots, N$) when referred to the simulated data sets in general.

Table 1
A short explanation of the symbols that are used throughout this paper.

Symbol	Explanation
A	Population specific atlas, fundamental dataset of the framework
A^*_p	P atlases containing apathology
A'_h	H atlas data sets containing inter-subject variability
A'_p	P atlas data sets containing pathology and inter-subject variability
E	Eigenvectors of the $K\times K$ matrix
h	$h=1,\ldots,H$
H	Number of simulated healthy subject DTI data sets
i	$i=1,\ldots,N$
I	Affinely transformed images to MNI space
$\tilde{I}$	Non-rigidly transformed data sets I to the population specific atlas space
K	Number of DTI data sets that issued to calculate the inter-subject variability
l	Number of estimated DT parameters
Λ	Eigenvalues of the $K\times K$ matrix
M	$K\times 2V$ matrix containing all data for the estimation of the inter-subject variability
N	Total number of simulated DTI data sets: $N=H+P$
O	Originally acquired DTI data sets
p	$p=1,\ldots,P$
P	Number of simulated pathology subject DTI data sets
Q_k	K data sets transformed to the atlas A to estimate the inter-subject variability
R	$K\times 1$ vector defined as zero-mean, unit variance, Gaussian distributed variables
r_o	Noise reduction factor of the processing pipeline
r_t	Theoretical noise due to estimating DTs from the DW images
S'_h	H simulated healthy subject DTI data sets in native space
S'_p	P simulated pathology subject DTI data sets in native space
S_h	H simulated healthy subject DTI data sets in native space with appropriate level of noise
S_p	P simulated pathology subject DTI data sets in native space with appropriate level of noise
σ_a	Noise that has to be added to simulated data sets
σ_f	Level of noise in simulated images after adding σ_n to original data sets
σ_n	Level of added Rician noise on original data sets to estimate noise reduction of processing pipeline
σ_o	Estimated noise level on the original DTI data sets
T	Deformation field
T_{hA}	H deformation fields from the atlas to the H images I_h
T_{pA}	P deformation fields from the atlas to the P images I_p
u	Number of DW images in one DTI data set
V	Number of atlas voxels for which FA>0.2

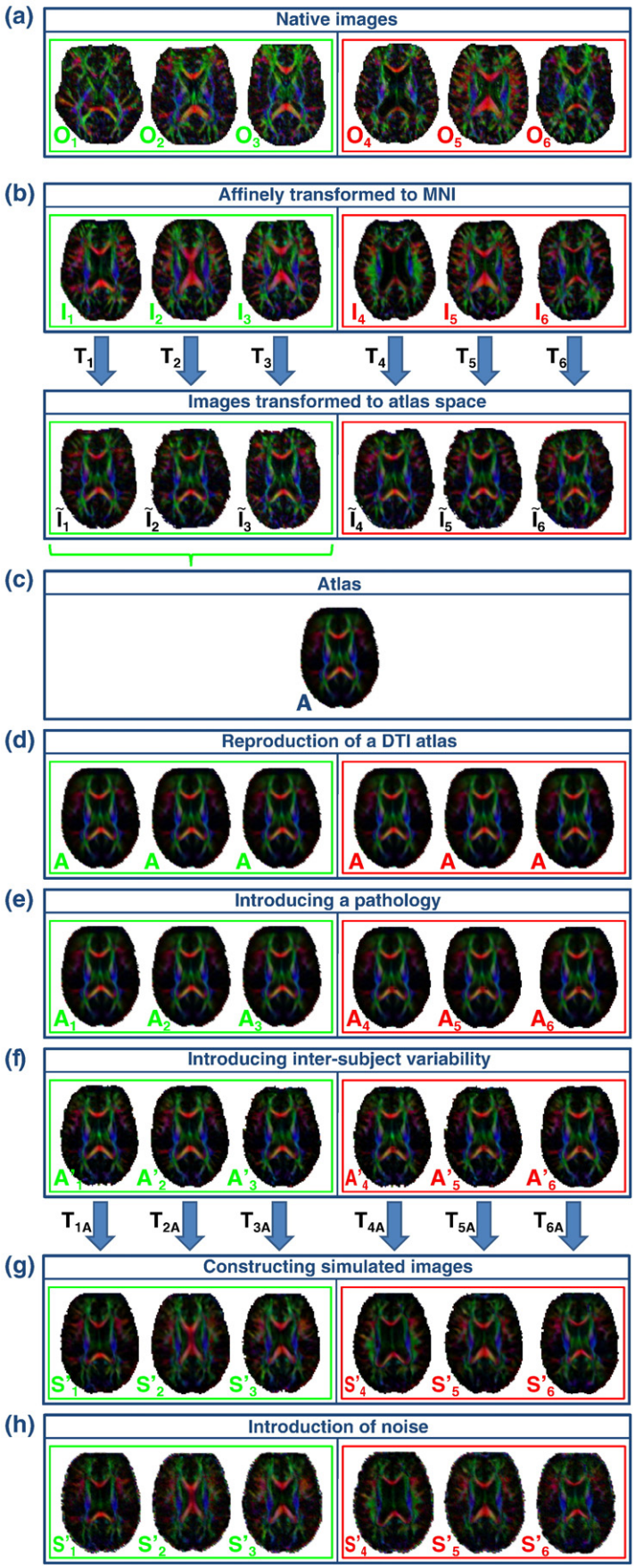

Fig. 2. In (a), axial FA slices of six randomly selected native DTI data sets are shown. Three of these images, O_1, O_2, and O_3, are healthy subject DTI data sets. On the other hand, images O_4, O_5, and O_6, are obtained from MS patients. In (b)–(i), the processing pipeline is illustrated using these data sets. Finally, in (i), the simulated images in affine space are visualized. Notice that these should resemble the native DTI data sets in affine space, as shown in (b).

Introducing noise

In order to obtain realistic, simulated DTI data sets, a realistic amount of noise should be included in the images. To this end, the noise level in the native images is estimated with the method described in Sijbers et al., (2007). In their approach, a histogram of the Rayleigh distributed background intensities of the DW images is used to estimate the noise level, which will be referred to as σ_o. A similar noise level should be observed in the simulated images. In order to obtain realistic, simulated DTI data sets, a realistic amount of noise should be added to the DW images of the simulated data set S' (in native space). In addition, since the noise is Rice distributed in MRI, realistic noise in the resulting simulated images also needs to be Rice distributed (Henkelman, 1985; Gudbjartsson and Patz, 1995).

The noise level is reduced in the simulated data sets due to the complete processing pipeline that is used to construct these images. One of the sources of this noise reduction is the interpolation step during the image transformation (Rohde et al., 2005). In addition, the noise is reduced since an averaged atlas is used as the fundamental data set in the ground truth method. Finally, an important noise reduction is caused by the decreased dimensionality in parameter space when the diffusion tensors are calculated from the DW images.

In order to calculate the noise level that has to be added to the simulated DTI data sets S_i, the noise reduction during the processing pipeline should be estimated. To this end, extra Rician noise with variance σ_n^2 is added to the DW images of the native data sets O_i. These data sets are subsequently used to construct the simulated DTI data sets S_in as described in the previous paragraphs. Thereafter, the resulting noise variance is estimated from the difference between the original simulated data sets S_i and the simulated data sets S_in that were constructed from original images O_i with extra noise:

$$\sigma_f^2 = \mathbb{E}\left[\left(S'^n_i - S'_i\right)^2\right], \tag{3}$$

in which the expectation E was replaced by a regional average. Finally, the noise reduction factor of this processing pipeline is computed as $r_o = \sigma_n/\sigma_f$.

To obtain simulated DW images with a similar noise standard deviation as in the original images O_i (i.e. σ_o), the amount of noise that has to be added (σ_a) to the simulated data sets, is given by:

$$\sigma_a = \sqrt{\sigma_o^2 - (\sigma_o / r_o)^2}. \tag{4}$$

However, it is important to note that the noise already present in S_i can be explained by the diffusion tensors, i.e., it completely adds to the variance of the diffusion tensor estimates. Since in the further processing, the DTs and not the DW images are of interest, the final noise level of the simulated DTs should be equal to the noise level of the DTs computed from the original images O_i. Since the dimensionality in parameter space is reduced by estimating the DTs from the DW images, a theoretical noise reduction r_t is expected:

$$r_t = \sqrt{u/l}, \tag{5}$$

with u the number of DW images and l the number of estimated DT parameters. Taking into account the reduction factor r_t, the noise standard deviation that has to be added to S_i becomes:

$$\sigma_a = \sqrt{\sigma_o^2 - (\sigma_o . r_t / r_o)^2}. \tag{6}$$

After adding the Rician distributed noise with noise level σ_a to the DW images of simulated data sets S'_h and S'_p, they are referred to as S_h and S_p, respectively.

The resulting simulated healthy subject and pathology data sets, which contain a realistic amount of noise, are referred to as S_h ($h = 1, \ldots, H$) and S_p ($p = 1, \ldots, P$), respectively, or as S_i ($i = 1, \ldots, H+P$) in general.

Subjects and data acquisition

In this work, 100 DTI data sets were acquired on a 1.5 T MR system. 80 of these images were obtained from a healthy subject group (age range: 18–65 years, 32 M, 48 F). In addition, 20 data sets were obtained from patients with Multiple Sclerosis (MS) (age range: 20–42 years, 6 M, 14 F).

Axial diffusion tensor images were obtained using an SE-EPI sequence with the following acquisition parameters: TR: 10.4 s; TE: 100 ms; diffusion gradient: 40 mT m^{-1}; FOV = 256×256 mm^2; number of slices = 60; voxel size = 2×2×2 mm^3; b = 700 s mm^{-2}; acquisition time: 12 min 18 s. Diffusion measurements were performed along 60 directions with 10 b_0-images and a nonlinear diffusion tensor estimation procedure was used based on the Levenberg–Marquardt optimization method (Jones, 2004b). DTI post-processing and visualization were performed with the diffusion toolbox 'ExploreDTI' (Leemans et al., 2009).

Examining the effect of image alignment and tissue degradation on VBA results

40 simulated data sets were generated with a specific level of noise and inter-subject variability to investigate the effect of coregistration and level of pathology on the sensitivity of the VBA results. Several levels of pathology (predefined increase of the transverse eigenvalues $\lambda_\perp$) were simulated in the splenium of the corpus callosum (size: 54 voxels in 4 consecutive axial slices) for 20 data sets (Ardekani et al., 2003; Barnea-Goraly et al., 2003; Park et al., 2004; Simon et al., 2005; Kyriakopoulos et al., 2007; Douaud et al., 2007).

Two VBA analyses were performed demonstrating the subtle changes in outcome of regions with a significant FA difference between healthy and diseased subjects due to imperfections in coregistration:

Analysis 1:. The predefined deformation fields to transform the simulated data sets to native space were applied to invert the data back to atlas space. In doing so, perfect spatial alignment is guaranteed taking into account the effects of data interpolation, allowing for the computation the effective levels of pathology (that is, prior to adding noise and inter-subject variability).

Analysis 2:. The data sets in native space (as in Analysis 1, but with noise and inter-subject variability added) are coregistered to the atlas using the non-rigid coregistration approach (Van Hecke et al., 2007).

For both analyses, the FA data were smoothed with a Gaussian kernel (3 mm FWHM) and a parametric t-test (the data were normally distributed according to the Lilliefors test) was used to compare the FA values between the healthy and the pathology data sets, followed by the Benjamini–Hochberg post-hoc correction for multiple comparisons (Benjamini and Hochberg, 1995). To quantify the VBA results, the sensitivity – calculated as the ratio of the number of true positives with the sum of the number of true positives and false negatives – is computed for both analyses and repeated 10 times, whereby the noise distribution as well as the inter-subject variability distribution is re-sampled.

Experiments and results

From the 100 ($=H+P+K$) acquired DTI data sets, 20 ($=P$) were obtained from pathology subjects with MS. The 20 ($=H$) healthy subject data sets were age- and sex-matched with the MS patient images. The remaining 60 ($=K$) healthy subject data sets were used to construct the inter-subject variability maps.

Native images

To illustrate the processing pipeline of the ground truth method, axial FA slices of six randomly selected native DTI data sets, colour

	WM structure	significant in these articles	number of voxels
(a)	Cerebellar peduncle	• Park et al. 2004 • Seok et al. 2007 • Kyriakopoulos et al. 2007	187
(b)	Cortico-spinal tract	• Sach et al. 2004 • Douaud et al. 2007 • Sage et al. 2007	90
(c)	Inferior longitudinal fasciculus	• Park et al. 2004 • Hubl et al. 2004 • Boronni et al. 2007	95
(d)	Cerebral peduncle	• Xie et al. 2005	54
(e)	Internal capsule	• Nagy et al. 2003 • Sage et al. 2007 • Sach et al. 2004 • Xie et al. 2005 • Kubicki et al. 2005 • Buchsbaum et al. 2006	76
(f)	Genu of the corpus callosum	• Ardekani et al. 2003 • Douaud et al. 2007 • Barnea-Goraly et al. 2003 • Anjari et al. 2007	50
(g)	Forceps minor	• Xie et al. 2005	115
(h)	External capsule	• Molko et al. 2004 • Barnea-Goraly et al. 2003	76
(i)	Splenium of the corpus callosum	• Simon et al. 2005 • Park et al. 2004 • Ardekani et al. 2003 • Douaud et al. 2007 • Barnea-Goraly et al. 2003 • Kyriakopoulos et al. 2007	70
(j)	Forceps major	• Agartz et al. 2001 • Kyriakopoulos et al. 2007	40
(k)	Corona Radiata	• Sach et al. 2004	136
(l)	Body of the corpus callosum	• Ardekani et al. 2003 • Douaud et al. 2007 • Barnea-Goraly et al. 2003 • Xie et al. 2005	44
(m)	Superior longitudinal fasciculus	• Seok et al. 2007 • Xie et al. 2005 • Kubicki et al. 2005 • Boronni et al. 2007 • Padovani et al. 2005 • Buchsbaum et al. 2006 • Kyriakopoulos et al. 2007	96
(n)	cingulum	• Park et al. 2004 • Kubicki et al. 2005 • Seok et al. 2007	42

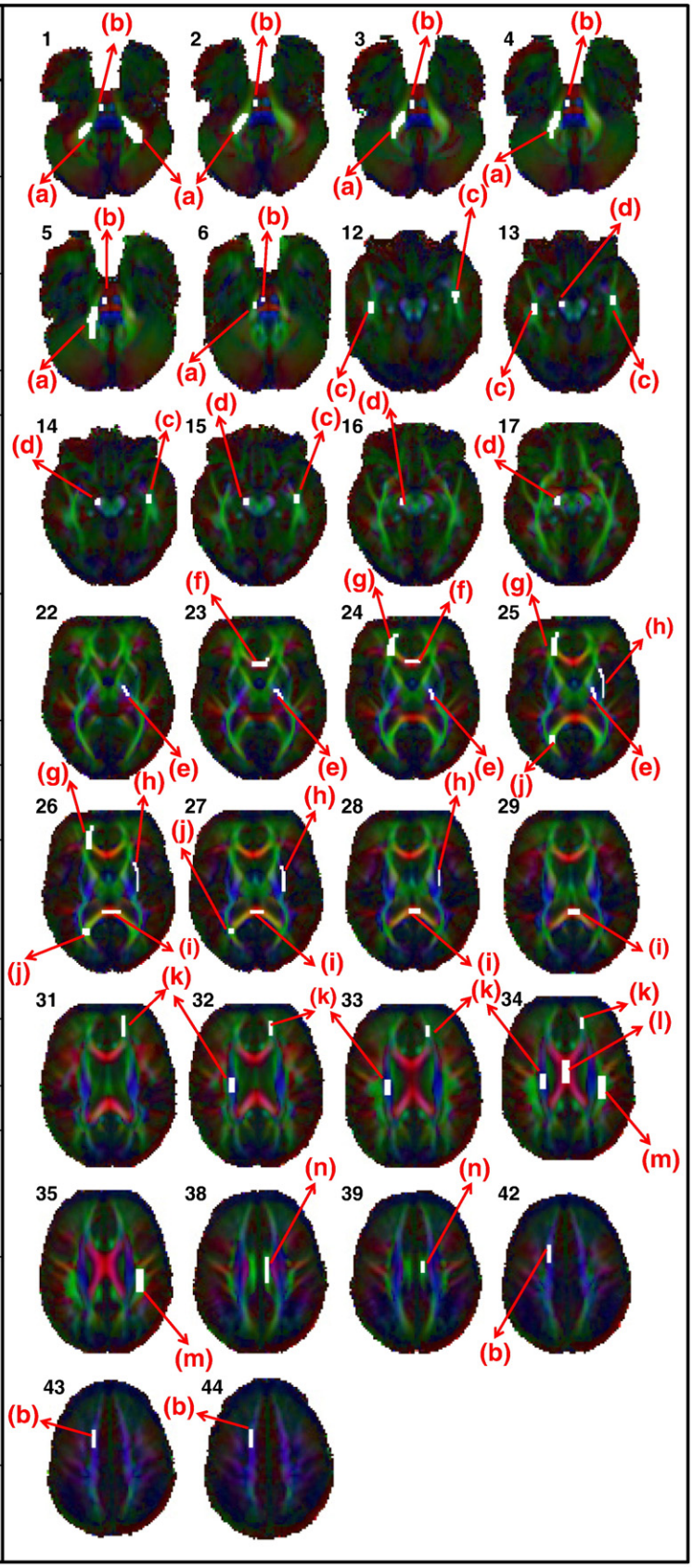

Fig. 3. On the left, different WM structures are displayed in which a simulated pathology is introduced. For each WM structure, the number of voxels in which a pathology is introduced is given for this example. In addition, references of studies are given that found a significant difference of the diffusion properties in this specific WM structure. The voxels in which the diffusion properties are altered are marked in white on the different axial slices of the DTI atlas.

encoded for the main diffusion direction, are displayed in Fig. 2a. Three of these (left) were acquired from healthy volunteers, whereas the other three (right) were obtained from MS patients.

Atlas construction

A population specific atlas was constructed from the native DTI data sets, as explained in the Methods section. As illustrated in Fig. 2b, these data sets were warped affinely to MNI space, followed by the transformation to the atlas space by the use of averaged deformation fields. Thereafter, an atlas was computed with a minimal deformation to all images of the subject group, as shown in Fig. 2c (Van Hecke et al., 2008). This DTI atlas, which is regarded as the fundamental data set of the ground truth method, was reproduced 40 ($=H+P$) times (see Fig. 2d).

Introducing pathology

Based on the reported results in the DTI literature, a predefined microstructural breakdown was introduced in different voxel clusters of the simulated pathology data sets (see Fig. 2e). As can be seen in Fig. 3, these selected WM structures and voxel clusters are coloured in white on different axial slices of the atlas data set. References to DTI studies in which the diffusion measures in these WM structures were observed to be significantly different between control subjects and patients are added to this Fig. (Park et al., 2004; Anjari et al., 2007; Sach et al., 2004; Sage et al., 2007; Hubl et al., 2004; Borroni et al., 2007; Xie et al., 2006; Nagy et al., 2003; Molko et al., 2004; Simon et al., 2005; Padovani et al., 2006; Seok et al., 2007; Kyriakopoulos et al., 2007; Douaud et al., 2007; Kubicki et al., 2005; Buchsbaum et al., 2006; Barnea-Goraly et al., 2003; Ardekani et al., 2003). In addition, the number of voxels in which the diffusion properties are modified in this example are also presented in Fig. 3.

An example of different levels of tissue degradation in the splenium of the corpus callosum is given in Fig. 4a and enlarged in Fig. 4b. The corresponding tensors are displayed in Fig. 4c. The degree of microstructural breakdown is here defined as a percentage of the original longitudinal and transverse eigenvalues in each voxel.

Introducing inter-subject variability

Inter-subject variability was estimated from 60 ($=K$) healthy subject DTI data sets. Examples of the images in atlas space that include inter-subject variability of the diffusion properties are shown in Fig. 2f. In Fig. 5, the inter-subject variance of the longitudinal and transverse eigenvalues is depicted, as reflected by the coefficient of variation, which is the standard deviation map of an eigenvalue image, normalized by the average of the different eigenvalue images. An axial, coronal, and sagittal slice of the FA map is shown in Fig. 5a. In Fig. 5b, the inter-subject variance of the longitudinal eigenvalues is depicted for the same axial, coronal and sagittal slices. Analogously, the inter-subject variance of the transverse eigenvalues is visualized in Fig. 5c. A high inter-subject variance is depicted in a bright colour, whereas a low inter-subject variance is depicted in a dark colour.

Constructing the simulated data sets

After generating the simulated DTI data sets in atlas space, a predefined set of deformation fields is applied to these data sets to transform them to native space. (see Fig. 2g). A qualitative example of the image correspondence between the simulated and the native DTI data sets is shown in Fig. 6. In Fig. 6a, axial FA slices of five randomly selected native DTI data sets are displayed. Axial FA slices of the corresponding simulated data sets are visualized in Fig. 6b. After overlaying the blue coloured native FA image and the red coloured simulated FA map, corresponding voxels with similar FA values will be coloured purple, as visualized in Figs. 6c–e.

In order to obtain a quantitative measure of the spatial image correspondence between the native and the simulated data sets, ROIs were manually drawn in different WM structures on the both the native and the simulated data sets (see Fig. 7). First, these ROIs, delineating the capsula externa, corpus callosum, cerebellar peduncle,

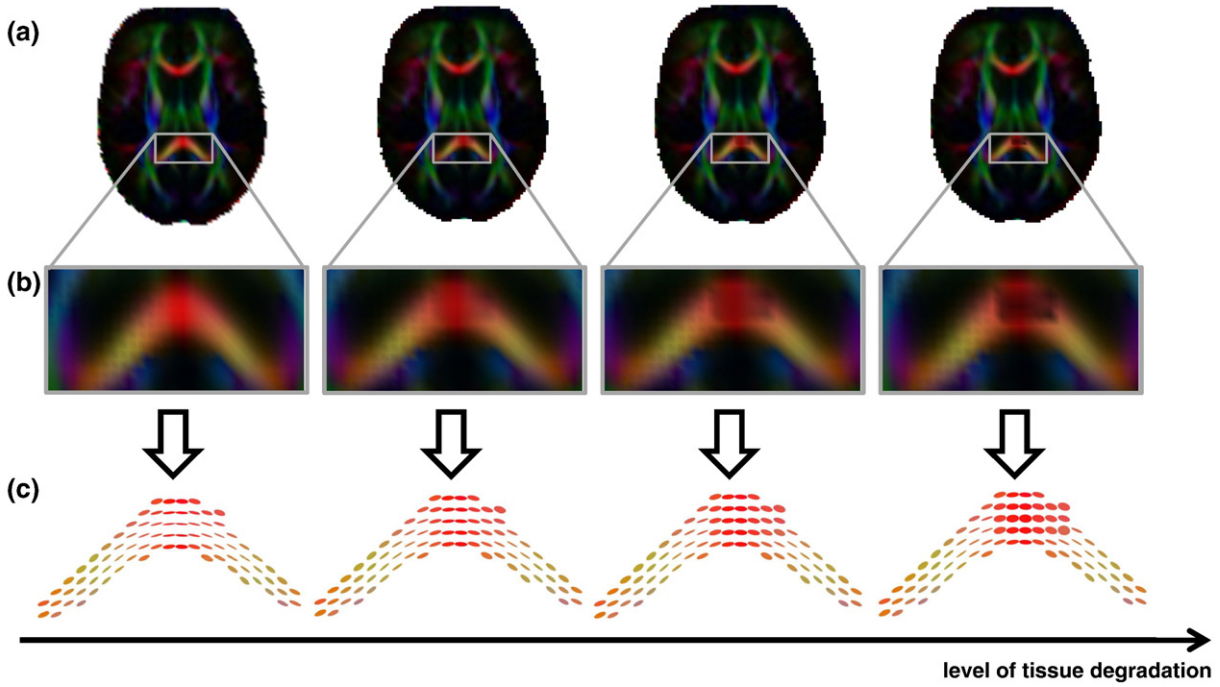

Fig. 4. An example is provided of the introduction of a pathology in the splenium of the corpus callosum. In (a), the axial slices are displayed for different levels of tissue degradation. The splenium is shown in more detail in (b). In (c), the diffusion ellipsoids of the splenium are visualized.

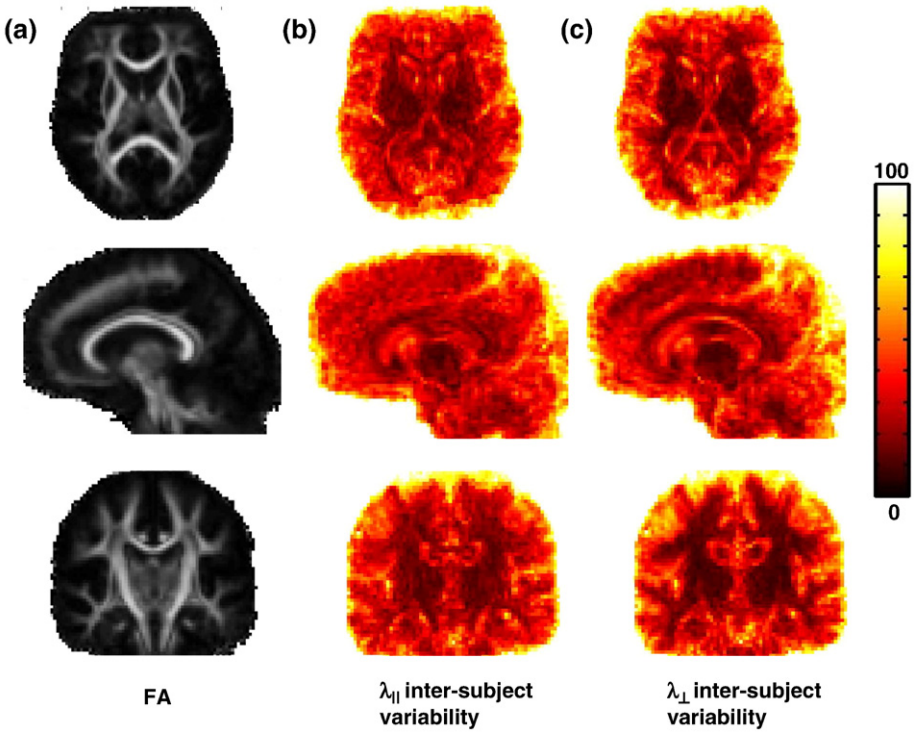

Fig. 5. In (a), an axial, sagittal, and coronal slice of the FA map are displayed. A measure of the inter-subject variability of the longitudinal and the transverse eigenvalues is shown in (b) and (c), respectively. This measure is calculated as the standard deviation of the eigenvalue images that result from the PCA analysis, weighted by the average of these images. High and low inter-subject variances are represented by a bright and a dark colour, respectively.

and posterior limb of the internal capsule, are drawn twice on the native data sets to test the reproducibility. These ROIs are marked in red and blue, as indicated in Fig. 7. Thereafter, the same WM structures are delineated on the simulated data sets, and marked in green. Finally, the red and blue voxels as well as the red and green voxels are overlaid. In the case that a voxel is selected by the red and the blue ROI, it will be given a purple colour, describing the reproducibility of the manual ROI delineation. Analogously, voxels appear yellow when they are present in both red and green ROIs, describing the image correspondence between the native and the simulated data sets. A quantitative measure for the ROI correspondence is calculated as the percentage of voxels that are present in both ROIs related to the total number of selected voxels in both ROIs. This measure is computed for the aforementioned ROIs in all 40 corresponding native and simulated data sets resulting in the boxplots of Fig. 7. The difference between both overlap measures was not statistically significant, demonstrating the high spatial correspondence between the simulated and the native DTI data sets for these large well-defined WM structures.

In order to evaluate the tensor correspondence between the native and the simulated data sets, the overlap of eigenvalue–eigenvector pairs (OVL) is computed (Basser and Pajevic, 2000). This measure calculates the scalar product between corresponding eigenvectors, weighted by the magnitude of the corresponding eigenvalues. The minimum value 0 indicates no overlap and the maximum value 1 represents complete overlap of the diffusion tensors. In Fig. 8a, the OVL measure between an native data set and its corresponding simulated data set is calculated for four randomly selected data sets and overlaid on the FA map of the native images. As can be observed in Fig. 8a, a high OVL is found in the major WM structures. In Fig. 8b, a histogram of the OVL values is displayed for these four data sets. All voxels with an FA value above 0.4 were included in this histogram. Finally, a scatter plot of the OVL and the FA values is displayed in Fig. 8c, demonstrating the high tensor correspondence in the major WM structures with a high FA.

Introducing noise

After applying the method of Sijbers et al. (2007) to the 40 native DTI data sets O_i, a noise level $\sigma_o = 18 \pm 1$ was found. Extra noise with a σ_i of 7 was added to the native images to estimate the observed noise reduction factor of the processing pipeline. After processing these images, the reduced noise level in the simulated data sets was observed to be $\sigma_f = 1.6$. Consequently, the noise reduction factor of the processing pipeline to construct the simulated data sets is $r_o = \sigma_i / \sigma_f = 4.3$.

In order to create simulated DT images that have the same noise level as the native images, extra noise has to be added to the DW images of data sets S_i. To obtain simulated DWI images with a similar noise level as in the original images (i.e. 18 ± 1), the noise that has to be added should have a $\sigma_a = \sqrt{\sigma_0^2 - (\sigma_o / r_o)^2} = 17.5$. However, as explained in the previous section, only the noise on the estimated diffusion tensors is important for the further processing and interpretation of the data sets. The variance of the noise that should be added to the simulated images therefore becomes $\sigma_a = \sqrt{\sigma_0^2 - (\sigma_o . r_t / r_o)^2} = 12.2$. Examples of simulated DTI data sets that include a realistic level of noise are visualized in Fig. 2h.

Examining the effect of image alignment and tissue degradation on VBA results

In Fig. 9, the VBA results of Analysis 1 and Analysis 2 are displayed for different levels of tissue degradation, expressed as a percentage of effective FA change. One of the axial slices, in which the pathology was simulated, is shown in Fig. 9a. In Fig. 9b, the VBA results of the splenium are shown qualitatively for analyses 1 and 2 for different levels of simulated pathology. The voxels, in which ground truth pathology was introduced, are given a purple colour. The subgroup of these voxels that were found as statistically significant in the VBA

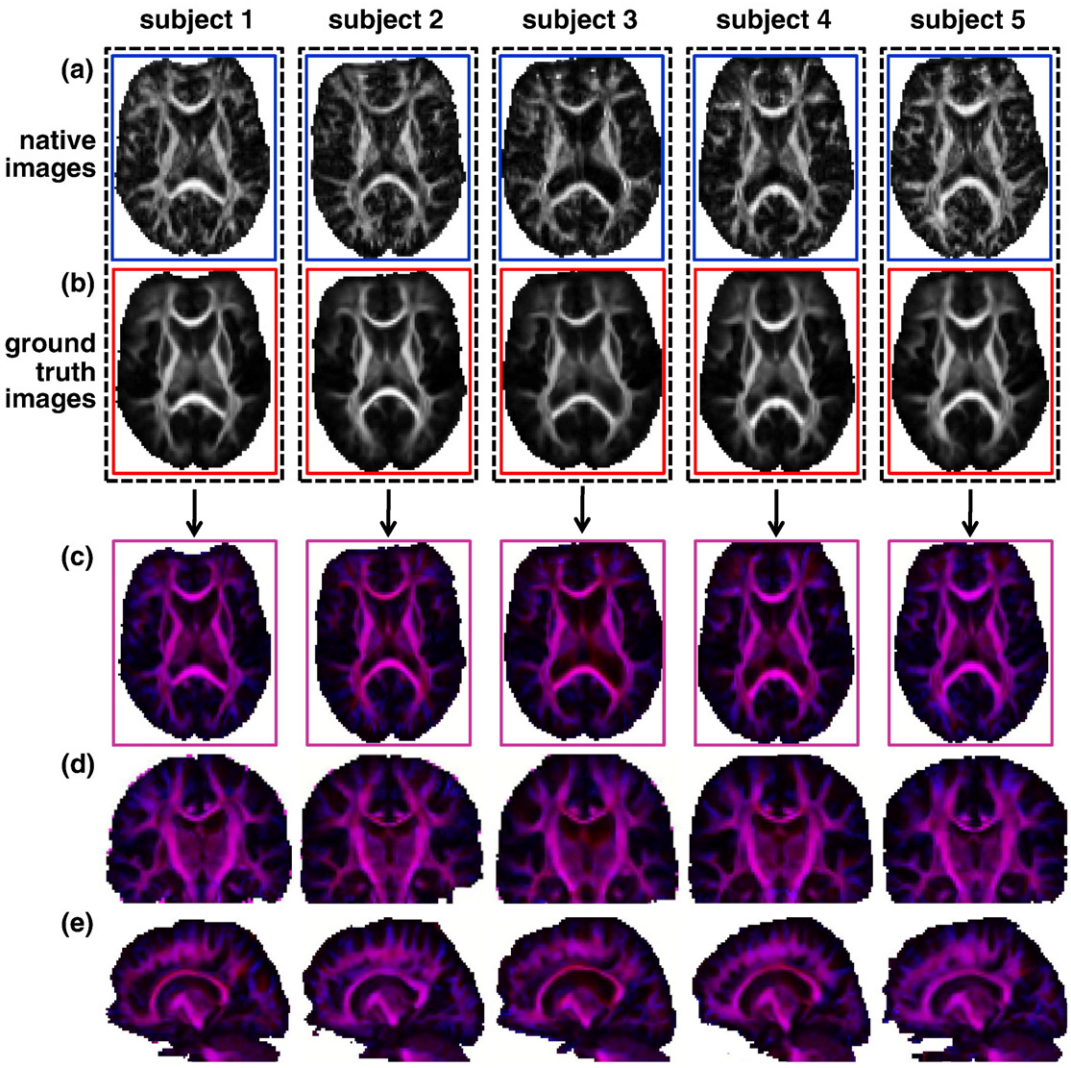

Fig. 6. The spatial image correspondence is represented visually for 5 randomly selected native data sets and their corresponding simulated data sets. The axial FA slices of these native and simulated data sets are visualized in (a) and (b), respectively. The FA maps of the native and the simulated data sets are colour encoded in blue and red, respectively. By overlaying these colour encoded images, the corresponding voxels with a similar FA value will be purple as can be seen on the axial, coronal, and sagittal slices, in (c), (d), and (e), respectively.

analysis are coloured in blue. For an effective FA decrease of 7%, 10%, 13%, 16%, 19%, and 21%, different results were obtained between both analyses: in Fig. 9c, these differences in sensitivity are displayed for the different levels of simulated pathology.

Discussion

In this work, a novel framework is presented for the construction of simulated DTI data sets, which include a predefined pathology. An increasing number of researchers apply VBA methods to analyse DTI data of control subjects and patients (Park et al., 2004; Anjari et al., 2007; Sach et al., 2004; Sage et al., 2007; Hubl et al., 2004; Borroni et al., 2007; Xie et al., 2006; Nagy et al., 2003; Molko et al., 2004; Simon et al., 2005; Padovani et al., 2006; Seok et al., 2007; Kyriakopoulos et al., 2007; Douaud et al., 2007; Kubicki et al., 2005; Ardekani et al., 2005; Buchsbaum et al., 2006; Barnea-Goraly et al., 2003; Ardekani et al., 2003). However, studies suggest that the VBA results are not always accurate and disease specific, since they depend on the parameter settings and implementations of the post-processing method (Jones et al., 2007; Zhang et al., 2007; Jones et al., 2005; Bookstein, 2001; Davatzikos, 2004). In this context, our framework allows one to estimate the accuracy, precision, and reliability of different post-processing approaches for detecting changes in diffusion properties with different predefined magnitudes and locations quantitatively.

The processing pipeline of the ground truth framework was based on the acquisition of 80 ($=H+K$) healthy subject and 20 ($=P$) MS patient DTI data sets. The MS patient data sets were included in the analysis in order to introduce morphological anomalies, such as enlarged ventricles or a thinned corpus callosum in our simulated data sets in order to increase the resemblance of the simulated study with realistic situations. For example, the inclusion of simulated DTI data sets with a morphological pathology in a VBA might hamper the coregistration accuracy, and thereby the reliability of the statistical analysis. However, it should be mentioned that the unknown alterations of the diffusion properties, which are present in the native DTI data sets of the MS patients, were not included in the simulated data sets. As such, the population specific atlas, which is considered as the fundamental image of our framework, only contains the diffusion information of the healthy subjects, although it is located in the atlas space of all subjects (i.e., both healthy subjects and MS patients).

As can be observed, for example, in Fig. 3, the population specific atlas particularly contains reliable information within the main WM structures. Since a large variability of the peripheral WM and the GM

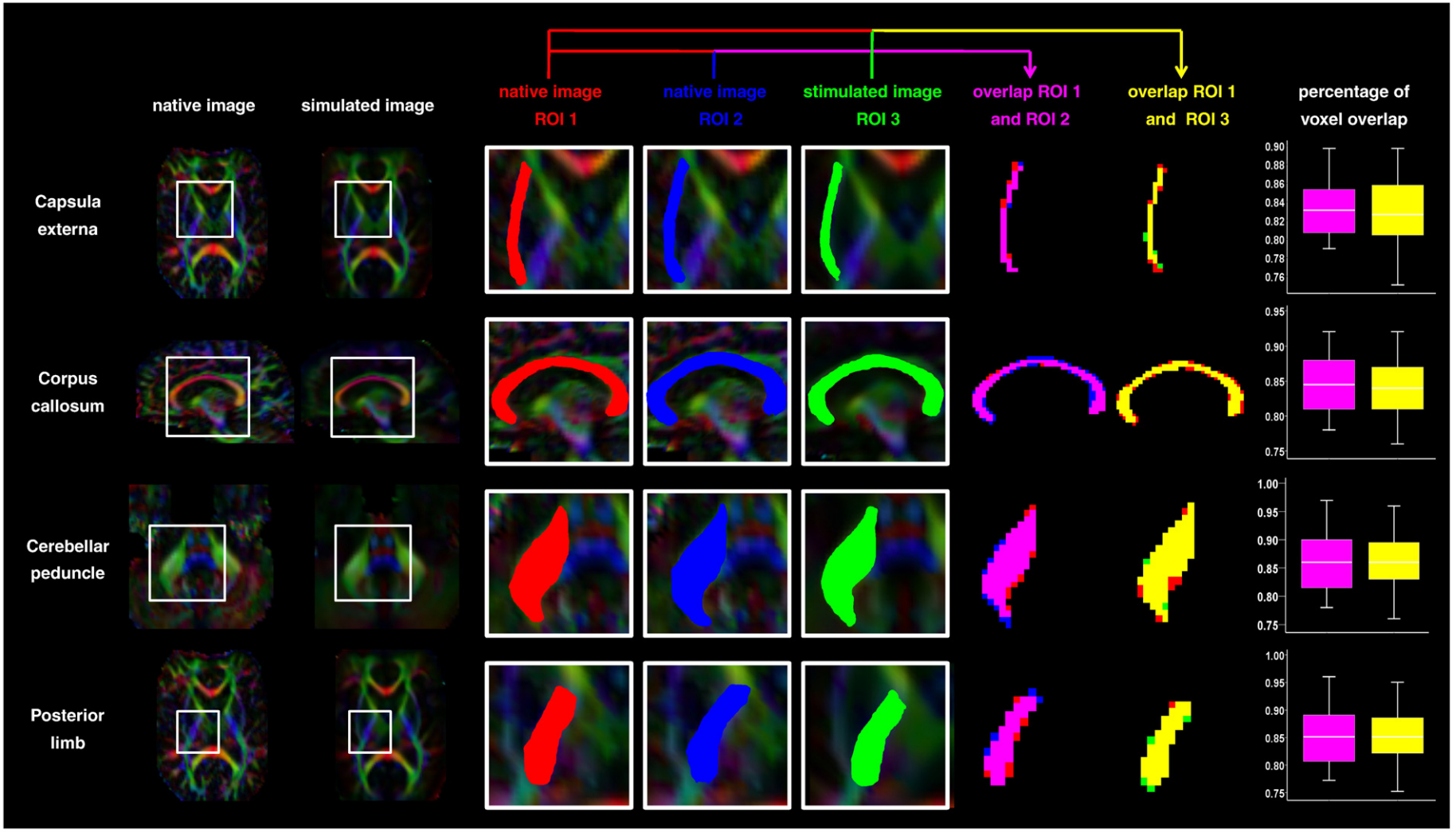

Fig. 7. ROIs are drawn twice in the capsula externa, the corpus callosum, the cerebellar peduncle, and the posterior limb of the native data sets, as displayed in red and blue. After overlaying these ROIs for each WM structure, voxels will appear purple, when they are included in both ROIs. The percentage of overlap is given on the right. Analogously, ROIs are delineated in the same WM structures of the simulated images, and displayed in green. The voxels that are included in the ROI of the native data set and of the simulated data set are then coloured yellow. Again, the percentage of overlap of these ROIs are shown on the right for the different WM structures.

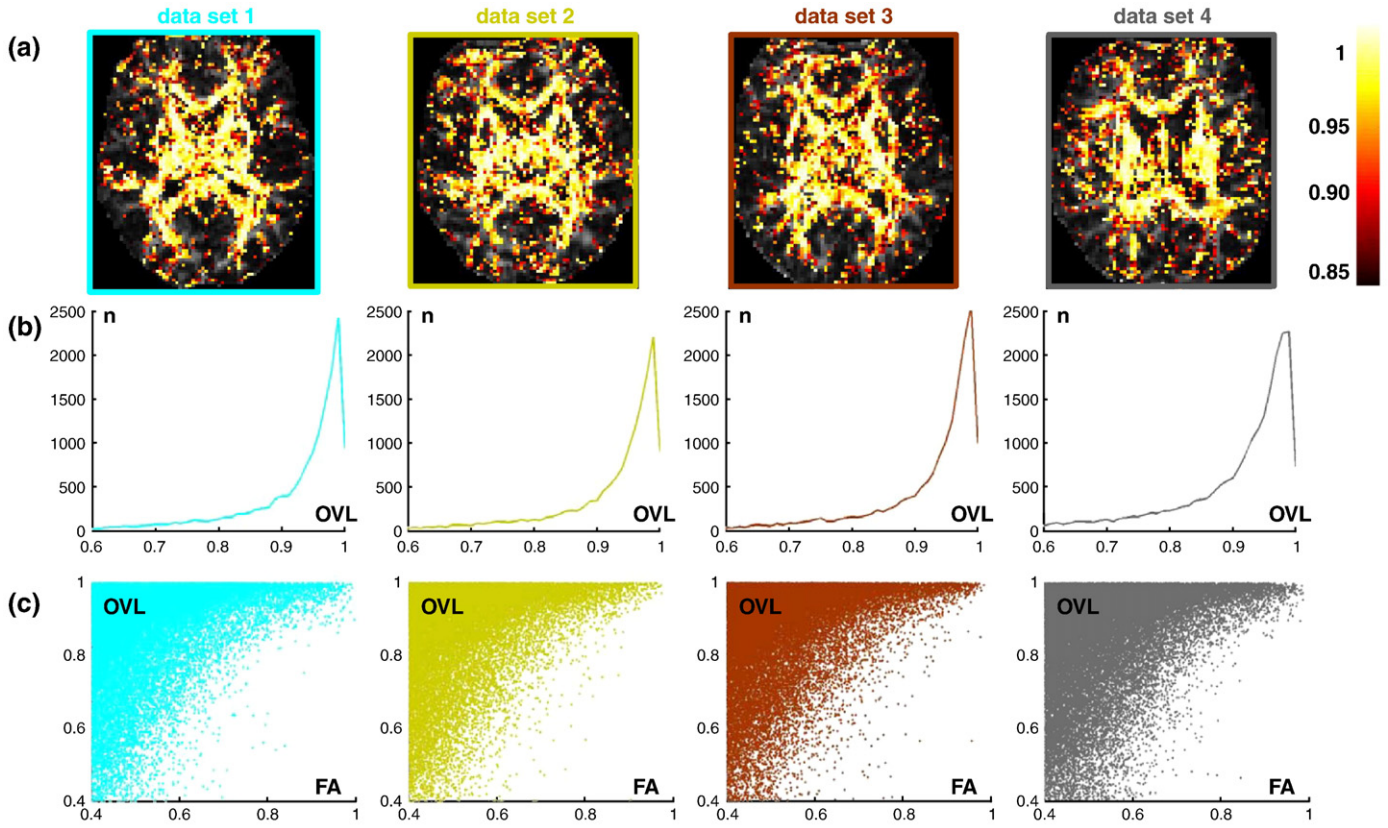

Fig. 8. The overlap of eigenvalue and eigenvector pairs (OVL) is calculated between 4 native images and their corresponding simulated data sets. In (a), this OVL measure is superimposed on the axial FA slices of the native data sets. A histogram of this OVL is calculated including all voxels with an FA>0.4, as shown in (b). In (c), a scatter plot of the OVL measure and the FA value is displayed, demonstrating the higher tensor correspondence in WM structures with a high FA.

structures exists in the DTI data sets across different subjects, this information is less reliable in the atlas. This large inter-subject variability is also illustrated in Figs. 5b and c, showing the inter-subject variances, as calculated by a PCA analysis on 60 ($=K$) healthy subjects, of the longitudinal and transverse eigenvalue maps, respectively. Since these peripheral WM structures are not reliably present in the fundamental atlas data set, no pathology diffusion alterations are introduced in the peripheral WM structures of the simulated DTI data sets. In this context, it should be mentioned that in VBA studies of different pathologies, all results in the peripheral WM should be interpreted very cautiously.

Examples of voxel clusters, in which microstructural breakdown is simulated by changes in the diffusion characteristics, are visualized in Fig. 3. Obviously, the magnitude, the spatial location and size of the pathology can be chosen differently from this example and can be modified to address specific issues and validate specific hypotheses. In addition, the nature of the pathology (for example, constant MD and FA increase or MD and FA increase, etc.) can be modified to simulate specific pathologies. Furthermore, it should be mentioned that the exact location of the pathology can be varied across the pathology subjects to simulate more complex configurations.

After including a pathology and inter-subject variability, the simulated DTI data sets are still embedded in the population specific atlas space. In order to simulate a realistic situation, these DTI data sets should be located in a native space. To his end, deformation fields were used to transform the simulated data sets to their native space. Since, in this work, realistic deformation fields were adopted to transform the atlas image to the individual space, the spatial correspondence of the simulated data sets with realistic DT images will depend on the accuracy of these deformation fields. Therefore, inaccuracies in the image alignment to the native DT images are reduced by the use of a population specific DTI atlas as the fundamental DTI data set. The magnitude of the deformation fields from the atlas to the native images is then minimized, thereby reducing potential coregistration errors. To further minimize these image alignment inaccuracies, three different image normalization techniques were applied to estimate the deformation fields between the atlas and the native DTI data sets. These deformation fields were subsequently averaged and used to transform the simulated data sets to their native space. In addition, the use of averaged deformation fields prevents the generated transformations of being biased toward a family of deformations that can be generated by one particular warping algorithm. Finally, the use of averaged deformation fields to construct the simulated data sets enhances the tensor correspondence between the native data sets and the simulated images, since the effect of tensor reorientation inaccuracies is reduced (Van Hecke et al., 2007, 2008).

After the transformation of the DT images to an individual space and the subsequent addition of a realistic amount of noise, simulated DTI data sets are constructed. The images can then be used to quantitatively evaluate different DTI post-processing approaches, since all the aspects of the pathology are known a priori. In this way, different implementation issues and parameter settings of the VBA methods can be examined separately. As shown by our example (Analysis 1 vs. Analysis 2), it is clear that the ground truth framework can be applied to investigate the effect of coregistration on the sensitivity of VBA results. Key to comparing a specific aspect of the VBA pipeline using this simulation approach is to keep all other predefined parameters and methods identical. In this example, for instance, when investigating the adverse effects of coregistration, not only the levels of noise and inter-subject variability, the size of smoothing kernel, and the applied statistical tests were the same, also

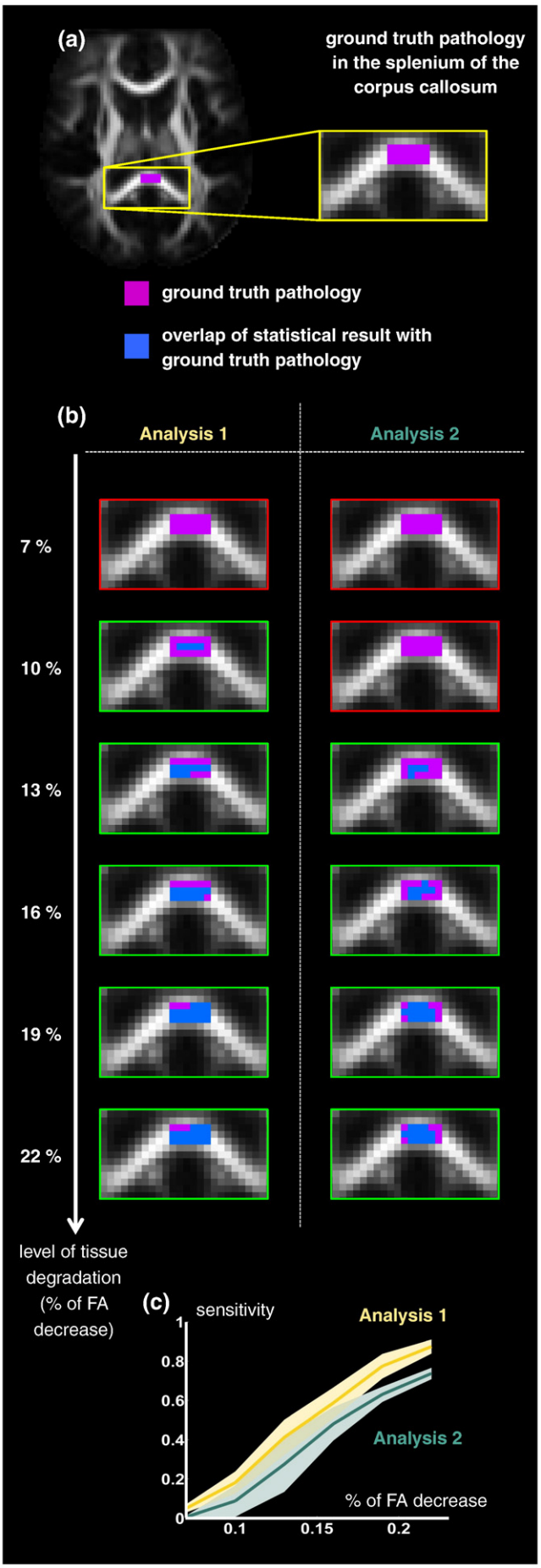

the actual transformation steps were included to consider the partial volume averaging artifacts due to interpolation, which are also present during actual coregistration. The analysis was also restricted to the splenium of the corpus callosum. Although not shown in this manuscript, other WM structures showed similar but non-trivial behavior, mainly being dependent on both the shape and size of the induced pathology and the WM structure itself. With these simulated VBA analyses, coregistration methods can be compared or even optimized by fine-tuning user-defined parameters.

The proposed framework for simulating DTI data sets serves to evaluate the effect of different DTI processing strategies – and their parameter settings – on the sensitivity and specificity of VBA results. In principle, the following general aspects and processing steps within such a DTI based VBA pipeline can be investigated:

- The applied diffusion gradient sampling scheme (Jones, 2004a);
- Motion and distortion correction of the DW images, e.g., with or without b-matrix rotation (Leemans and Jones, In press);
- Diffusion tensor estimation approaches (Koay et al., 2006);
- DTI coregistration for spatial normalization and atlas construction;
- Data smoothing (the DW images, the tensor components, the FA maps, etc.);
- Application of parametric vs. non-parametric statistics;
- Post-hoc analyses, such as multiple comparisons correction.

Each these processing steps (each with their own set of 'tunable' parameters) will contribute to the overall variability (in terms of accuracy and precision) of the final VBA result. Note, however, that it is important to realize that their relative contribution in this variability may differ significantly. In this context, this simulation framework will help to identify the bottlenecks in the VBA pipeline (e.g., the choice of the kernel size for data smoothing may affect the VBA outcome more than the choice of the diffusion tensor estimation approach).

Despite its virtues, the presented framework of constructing realistic, simulated DTI data sets has some limitations. In our study, only the longitudinal and transverse eigenvalues can be altered to simulate the assumed effects of axonal degeneration and demyelination, respectively. However, the exact relation between microstructural breakdown and diffusion tensor properties is not known, partly due to the inadequacy of DTI to resolve multiple fiber populations. In addition, in the pathology simulation, radial diffusion symmetry is assumed, i.e., the second and third eigenvalues are changed in the same way. Furthermore, the diffusion orientation information, reflected by the eigenvectors, are not altered. Another limitation is that the inter-subject variability was estimated using a procedure in which a Gaussian distribution was assumed. Although this assumption cannot be verified directly, we believe that this Gaussianity may still be valid by using a large amount of data sets for the estimation of a realistic inter-subject variability. Finally, since deformation fields between the atlas and the native data sets were used to construct the simulated images, the spatial information of these simulated images is defined by the native data sets. In future work, we intend to generalize this procedure by increasing the number of native data sets for the construction of more simulated data sets, as described in Xue et al. (2006).

Fig. 9. VBA results for a ground truth pathology in the splenium of the corpus callosum. In (a), the ground truth pathology is shown on an axial slice of the atlas FA map. The VBA results after a simulated perfect spatial alignment (Analysis 1) and after non-rigid coregistration (Analysis 2) are visualized in (b). The voxels in which a ground truth pathology is introduced are coloured in purple, whereas the significant voxels are coloured in blue. In (c), the VBA sensitivity is displayed for different levels of tissue degradation, as presented by the corresponding effective FA decrease.

Conclusion

In this work, a framework for constructing simulated DTI data sets with a predefined pathology is presented. These data sets can be employed in studies to evaluate the accuracy, precision, and reproducibility of different VBA algorithms quantitatively. We are convinced that this will lead to an improved understanding of the reliability and shortcomings of these post-processing methods to study different WM altering pathologies.

References

Abe, O., Aokia, S., Hayashia, N., Yamadaa, H., Kunimatsua, A., Moria, H., Yoshikawaa, T., Okubob, T., Ohtomoa, K., 2002. Normal aging in the central nervous system: quantitative MR diffusion-tensor analysis. Neurobiol. Aging 23 (3), 433–441.

Agartz, I., Andersson, J.L.R., Skare, S., 2001. Abnormal brain white matter in schizophrenia: a diffusion tensor imaging study. NeuroReport 12 (10), 2251–2254.

Alexander, D.C., Pierpaoli, C., Basser, P.J., Gee, J.C., 2001. Spatial transformations of diffusion tensor magnetic resonance images. IEEE. Trans. Med. Imaging 20 (11), 1131–1139.

Anjari, M., Srinivasan, L., Allsop, J.M., Hajnal, J.V., Rutherford, M.A., Edwards, A.D., Counsell, S.J., 2007. Diffusion tensor imaging with tract-based spatial statistics reveals local white matter abnormalities in preterm infants. NeuroImage 35 (3), 1021–1027.

Ardekani, B.A., Bappal, A., D'Angelo, D., Ashtari, M., Lencz, T., Szeszko, P.R., Butler, P.D., Javitt, D.C., Lim, K.O., Hrabe, J., Nierenberg, J., Branch, C.A., Hoptman, M.J., 2005. Brain morphometry using diffusion weighted MRI: application to schizophrenia. NeuroReport 16 (13), 1455–1459.

Ardekani, B.A., Nierenberg, J., Hotman, M.J., Javitt, D.C., Lim, K.O., 2003. MRI study of white matter diffusion anisotropy in schizophrenia. NeuroReport 14 (16), 2025–2029.

Ashburner, J., Friston, K.J., 1999. Nonlinear spatial normalization using basis functions. Hum. Brain Mapp. 7 (4), 254–266.

Ashburner, J., Friston, K.J., 2000. Voxel-based morphometry — the methods. NeuroImage 11, 805–821.

Bammer, R., Augustin, M., Strasser-Fuchs, S., Seifert, T., Kapeller, P., Stollberger, R., Ebner, F., Hartung, H.P., Fazekas, F., 2000. Magnetic resonance diffusion tensor imaging for characterizing diffuse and focal white matter abnormalities in multiple sclerosis. Magn. Reson. Med. 44 (4), 583–591.

Barnea-Goraly, N., Eliez, S., Hedeus, M., Menon, V., White, C., Moseley, M., Reiss, A.L., 2003. White matter tract alterations in fragile X syndrome: preliminary evidence from diffusion tensor imaging. Am. J. Med. Genet., B. Neuropsychiatr. Genet. 118 (1), 81–88.

Basser, P.J., Mattiello, J., Le Bihan, D., 1994. MR diffusion tensor spectroscopy and imaging. Biophys. J. 66 (1), 259–267.

Basser, P.J., Pajevic, S., 2000. Statistical artifacts in diffusion tensor MRI (DT-MRI) caused by background noise. Magn. Reson. Med. 44 (1), 41–50.

Basser, P.J., Pajevic, S., Pierpaoli, C., Duda, J., Aldroubi, A., 2000. In vivo fiber tractography using DT-MRI data. Magn. Reson. Med. 44, 625–632.

Beaulieu, C., 2002. The basis of anisotropic water diffusion in the nervous system — a technical review. NMR Biomed. 15 (7–8), 435–455.

Benjamini, Y., Hochberg, Y., 1995. Controlling the false discovery rate: a practical and powerful approach to multiple testing. J. Roy. Statist. Soc. Ser. B (57), 289–300.

Bookstein, F.L., 2001. Voxel-based morphometry" should not be used with imperfectly registered images. NeuroImage 14 (6), 1454–1462.

Borroni, B., Brambati, S.M., Agosti, C., Gipponi, S., Bellelli, G., Gasparotti, R., Garibotto, V., Di Luca, M., Scifo, P., Perani, D., Padovani, A., 2007. Evidence of white matter changes on diffusion tensor imaging in frontotemporal dementia. Arch. Neurol. 64 (2), 246–251.

Bozzali, M., Cherubini, A., 2007. Diffusion tensor MRI to investigate dementias: a brief review. Magn. Reson. Imaging 25 (6), 969–977.

Buchsbaum, M.S., Friedman, J., Buchsbaum, B.R., Chu, K., Hazlett, E.A., Newmark, R., Schneiderman, J.S., Torosjan, Y., Tang, C., Hof, P.R., Stewart, D., Davis, K.L., Gorman, J., 2006. Diffusion tensor imaging in schizophrenia. Biol. Psych. 60 (11), 1181–1187.

Budde, M.D., Kim, J.H., Liang, H.-F., Schmidt, R.E., Russell, J.H., Cross, A.H., Song, S.-K., 2007. Toward accurate diagnosis of white matter pathology using diffusion tensor imaging. Magn. Reson. Med. 57 (4), 688–695.

Burns, J., Job, D., Bastin, M.E., Whalley, H., Macgillivray, T., Johnstone, E.C., Lawrie, S.M., 2003. Structural disconnectivity in schizophrenia: a diffusion tensor magn reson imaging study. Br. J. Psychiatry 182, 439–443.

Catani, M., 2006. Diffusion tensor magn reson imaging tractography in cognitive disorders. Curr. Opin. Neurol. 19 (6), 599–606.

Cercignani, M., Bozalli, M., Iannucci, G., Comi, G., Filippi, M., 2002. Intra-voxel and inter-voxel coherence in patients with multiple sclerosis assessed using diffusion tensor MRI. J. Neurol. 249 (7), 875–883.

Cherubini, A., Luccichenti, G., Pran, P., Hagberg, G.E., Barba, C., Formisano, R., Sabatini, U., 2007. Multimodal fMRI tractography in normal subjects and in clinically recovered traumatic brain injury patients. Neuroimage 34 (4), 1331–1341.

Ciccarelli, O., Werring, D.J., Barker, G.J., Griffin, C.M., Wheeler-Kingshott, C.A.M., Miller, D.H., Thompson, A.J., 2003. A study of the mechanisms of normal-appearing white matter damage in multiple sclerosis using diffusion tensor imaging — evidence of Wallerian degeneration. J. Neurol. 250 (3), 287–292.

D'Agostino, E., Maes, F., Vandermeulen, D., Suetens, P., 2003. A viscous fluid model for multimodal non-rigid image registration using mutual information. Med. Image Anal. 7 (4), 565–575.

Davatzikos, C., 2004. Why voxel-based morphometric analysis should be used with great caution when characterizing group differences. NeuroImage 23 (1), 17–20.

Douaud, G., Smith, S., Jenkinson, M., Behrens, T., Johansen-Berg, H., Vickers, J., James, S., Voets, N., Watkins, K., Matthews, P.M., James, A., 2007. Anatomically related grey and white matter abnormalities in adolescent-onset schizophrenia. Brain 130 (Pt.9), 2375–2386.

Foong, J., Symms, M.R., Barker, G.J., Maier, M., Miller, D.H., Ron, M.A., 2002. Investigating regional white matter in schizophrenia using diffusion tensor imaging. NeuroReport 13 (3), 333–336.

Ge, Y., Law, M., Johnson, G., Herbert, J., Babb, J.S., Mannon, L.J., Grossman, R.I., 2004. Preferential occult injury of corpus callosum in multiple sclerosis measured by diffusion tensor imaging. J. Magn. Reson. Imaging 20 (1), 1–7.

Griffin, C.M., Chard, D.T., Ciccarelli, O., Kapoor, B., Barker, G.J., Thompson, A.I., Miller, D.H., 2001. Diffusion tensor imaging in early relapsing-remitting multiple sclerosis. Mult. Scler. 7 (5), 290–297.

Gudbjartsson, H., Patz, S., 1995. The Rician distribution of noisy MRI data. Magn. Reson. Med. 34, 910–914.

Harsan, L.A., Poulet, P., Guignard, B., Steibel, J., Parizel, N., de Sousa, P.L., Boehm, N., Grucker, D., Ghandour, M.S., 2006. Brain dysmyelination and recovery assessment by noninvasive in vivo diffusion tensor magn reson imaging. J. Neurosci. Res. 83 (3), 392–402.

Hasan, K.M., Gupta, R.K., Santos, R.M., Wolinsky, J.S., Narayana, P.A., 2005. Fractional diffusion tensor anisotropy of the seven segments of the normal-appearing white matter of the corpus callosum in healthy adults and relapsing remitting multiple sclerosis. J. Magn. Reson. Imaging 21 (6), 735–743.

Henkelman, R.M., 1985. Measurement of signal intensities in the presence of noise in MR images. Med. Phys. 12 (2), 232–233.

Hsu, J.-L., Leemans, A., Bai, C.-H., Lee, C.-H., Tsai, Y.-F., Chiu, H.-C., Chen, W.-H., 2008. Gender differences and age-related white matter changes of the human brain: a diffusion tensor imaging study. NeuroImage 39 (2), 566–577.

Hubl, D., Koenig, T., Strik, W., Federspiel, A., Kreis, R., Boesch, C., Maier, S.E., Schroth, G., Lovblad, K., Dierks, T., 2004. Pathways that make voices: white matter changes in auditory hallucinations. Arch. Gen. Psychiatry 61 (7), 658–668.

Huster, R., Westerhausen, R., Kreuder, F., Schweiger, E., Wittling, W., 2009. Hemispheric and gender related dierences in the midcingulum bundle: a DTI study. Hum. Brain Mapp. 30 (2), 383–391.

Jones, D.K., 2004a. The effect of gradient sampling schemes on measures derived from diffusion tensor MRI: a Monte Carlo study 51 (4), 4607–4621.

Jones, D.K., 2004b. The effect of gradient sampling schemes on measures derived from diffusion tensor MRI: a Monte Carlo study. Magn. Reson. Med. 51, 807–815.

Jones, D.K., Basser, P.J., 2004. Squashing peanuts and smashing pumpkins: how noise distorts diffusion-weighted MR data 52 (5), 979–993.

Jones, D.K., Chitnis, X.A., Job, D., Khong, P.L., Leung, L.T., Marenco, S., Smith, S.M., Symms, M.R., 2007. What happens when nine different groups analyze the same DT-MRI data set using voxel-based methods? Proc. ISMRM 15th Annual Meeting. Berlin, p. 74.

Jones, D.K., Symms, M.R., Cercignani, M., Howarde, R.J., 2005. The effect of filter size on VBM analyses of DT-MRI data. NeuroImage 26 (2), 546–554.

Karlsgodt, K.H., van Erp, T.G.M., Poldrack, R.A., Bearden, C.E., Nuechterlein, K.H., Cannon, T.D., 2007. Diffusion tensor imaging of the superior longitudinal fasciculus and working memory in recent-onset schizophrenia. Biol. Psych. 63 (5), 512–518.

Koay, C.G., Chang, L.C., Carew, J.D., Pierpaoli, C., Basser, P.J., 2006. A unifying theoretical and algorithmic framework for least squares methods of estimation in diffusion tensor imaging. J. Magn. Reson. 182 (1), 115–125.

Kubicki, M., Park, H., Westin, C.-F., Nestor, P.G., Mulkern, R.V., Maier, S.E., Niznikiewicz, M., Connor, E.E., Levitt, J.J., Frumin, M., Kikinis, R., Jolesz, F.A., McCarley, R.W., Shentona, M.E., 2005. DTI and MTR abnormalities in schizophrenia: analysis of white matter integrity. NeuroImage 26 (4), 1109–1118.

Kubicki, M., Westin, C.-F., Maier, S.E., Frumin, M., Nestor, P.G., Salisbury, D.F., Kikinis, R., Jolesz, F.A., McCarley, R.W., Shenton, M.E., 2002. Uncinate fasciculus findings in schizophrenia: a magnetic resonance diffusion tensor imaging study. Am. J. Psychiatry 159 (5), 813–820.

Kubicki, M., Westin, C.-F., Nestor, P.G., Wible, C.G., Frumin, M., Maier, S.E., Kikinis, R., Jolesz, F.A., McCarley, R.W., Shenton, M.E., 2003. Cingulate fasciculus integrity disruption in schizophrenia: a magnetic resonance diffusion tensor imaging study. Biol. Psych. 54 (11), 1171–1180.

Kumra, S., Ashtari, M., McMeniman, M., Vogel, J., Augustin, R., Becker, D.E., Nakayama, E., Gyato, K., Kane, J.M., Lim, K., Szeszko, P., 2004. Reduced frontal white matter integrity in early-onset schizophrenia: a preliminary study. Biol. Psych. 55 (12), 1138–1145.

Kyriakopoulos, M., Vyas, N.S., Barker, G.J., Chitnis, X.A., Frangou, S., 2007. A diffusion tensor imaging study of white matter in early-onset schizophrenia. Biol. Psych. 63 (5), 519–523.

Lee, S.-K., Kim, D.I., Kim, J., Kim, D.J., Kim, H.D., Kim, D.S., Mori, S., 2005. Diffusion-tensor MR imaging and fiber tractography: a new method of describing aberrant fiber connections in developmental CNS anomalies. RadioGraphics 25 (1), 53–68.

Leemans, A., Jeurissen, B., Sijbers, J., Jones, D., 2009. ExploreDTI: a graphical toolbox for processing, analyzing, and visualizing diffusion MR data. In: 17th Annual Meeting of Proc. Intl. Soc. Mag. Reson. Med., Hawaii, USA.

Leemans, A., Jones, D.K., In press. The B-matrix must be rotated when correcting for subject motion in DTI data. Magnetic Resonance in Medicine.

Leemans, A., Sijbers, J., De Backer, S., Vandervliet, E., Parizel, P.M., 2005a. Affine coregistration of diffusion tensor magnetic resonance images using mutual information. Lect. Notes Comput. Sci. 3708, 523–530.

Leemans, A., Sijbers, J., Verhoye, M., Van der Linden, A., Van Dyck, D., 2005b. Mathematical framework for simulating diffusion tensor MR neural fiber bundles. Magn. Reson. Med. 53 (4), 944–953.
Maes, F., Collignon, A., Vandermeulen, D., Marchal, G., Suetens, P., 1997. Multimodality image registration by maximization of mutual information. IEEE Trans. Med. Imaging 16 (2), 187–198.
Molko, N., Cachia, A., Rivi, ère, D., Mangin, J.-F., Bruandet, M., Le Bihan, D., Cohen, L., Dehaene, S., 2004. Brain anatomy in turner syndrome: evidence for impaired social and spatial-numerical networks. Cereb. Cort. 14 (8), 840–850.
Molko, N., Pappata, S., Mangin, J.F., Poupon, C., Vahedi, K., Jobert, A., LeBihan, D., Bousser, M.G., Chabriat, H., 2001. Diffusion tensor imaging study of subcortical gray matter in CADASIL. Stroke 32 (9), 2049–2054.
Nagy, Z., Westerberg, H., Skare, S., Andersson, J.L., Lilja, A., Flodmark, O., Fernell, E., Holmberg, K., Bohm, B., Forssberg, H., Lagercrantz, H., Klingberg, T., 2003. Preterm children have disturbances of white matter at 11 years of age as shown by diffusion tensor imaging. Pediatr. Res. 54 (8), 672–679.
Padovani, A., Borroni, B., Brambati, S.M., Agosti, C., Broli, M., Alonso, R., Scifo, P., Bellelli, G., Alberici, A., Gasparotti, R., Perani, D., 2006. Diffusion tensor imaging and voxel based morphometry study in early progressive supranuclear palsy. J. Neurol,. Neurosurgery,. and. Psychiatry. 77 (4), 457–463.
Park, H.-J., Westin, C.-F., Kubicki, M., Maier, S.E., Niznikiewicz, M., Baer, A., Frumin, M., Kikinis, R., Jolesz, F.A., McCarley, R.W., Shenton, M.E., 2004. White matter hemisphere asymmetries in healthy subjects and in schizophrenia: a diffusion tensor MRI study. NeuroImage 23 (1), 213–223.
Pfefferbaum, A., Sullivan, E.V., Hedehus, M., Adalsteinsson, E., Lim, K.O., Moseley, M., 2000. In vivo detection and functional correlates of white matter microstructural disruption in chronic alcoholism. Alcohol Clin. Exp. Res. 24, 1214–1221.
Rohde, G.K., Barnett, A.S., Basser, P.J., Pierpaoli, C., 2005. Estimating intensity variance due to noise in registered images: applications to diffusion tensor MRI. NeuroImage 26 (3), 673–684.
Rovaris, M., Filippi, M., 2007. Diffusion tensor MRI in multiple sclerosis. Magn. Reson. Imaging (Suppl. 1), 27S–30S.
Rueckert, D., Sonoda, L.I., Hayes, C., Hill, D.L., Leach, M.O., Hawkes, D.J., 1999. Nonrigid registration using free-form deformations: application to breast MR images. IEEE Trans. Med. Imaging 18 (8), 712–721.
Sach, M., Winkler, G., Glauche, V., Liepert, J., Heimbach, B., Koch, M.A., Bchel, C., Weiller, C., 2004. Diffusion tensor MRI of early upper motor neuron involvement in amyotrophic lateral sclerosis. Brain 127 (Pt.2), 340–350.
Sage, C.A., Peeters, R.R., Grner, A., Robberecht, W., Sunaert, S., 2007. Quantitative diffusion tensor imaging in amyotrophic lateral sclerosis. NeuroImage 34 (2), 486–499.
Schwartz, E.D., Cooper, E.T., Fan, Y., Jawad, A.F., Chin, C.L., Nissanov, J., Hackney, D.B., 2005. MRI diffusion coefficients in spinal cord correlate with axon morphometry. NeuroReport 16 (1), 73–76.
Seok, J.H., Park, H.J., Chun, J.W., Lee, S.K., Cho, H.S., Kwon, J.S., Kim, J.J., 2007. White matter abnormalities associated with auditory hallucinations in schizophrenia: a combined study of voxel-based analyses of diffusion tensor imaging and structural magn reson imaging. Psychiatry Res. 156 (2), 93–104.
Simon, T.J., Ding, L., Bish, J.P., McDonald-McGinn, D.M., Zackai, E.H., Gee, J., 2005. Volumetric, connective, and morphologic changes in the brains of children with chromosome 22q11.2 deletion syndrome: an integrative study. NeuroImage 25 (1), 169–180.
Sijbers, J., Poot, D., den Dekker, A.J., Pintjens, W., 2007. Automatic estimation of the noise variance from the histogram of a magnetic resonance image. Phys. Med. Biol. 52, 1335–1348.
Smith, S.M., Jenkinson, M., Johansen-Berg, H., Rueckert, D., Nichols, T.E., Mackay, C.E., Watkins, K.E., Ciccarelli, O., Cader, M.Z., Matthews, P.M., Behrens, T.E., 2006. Tract-based spatial statistics: voxelwise analysis of multi-subject diffusion data. NeuroImage 4 (31), 1487–1505.
Snook, L., Paulson, L.-A., Roy, D., Phillips, L., Beaulieu, C., 2005. Diffusion tensor imaging of neurodevelopment in children and young adults. NeuroImage 26 (4), 1164–1173.
Snook, L., Plewes, C., Beaulieu, C., 2007. Voxel based versus region of interest analysis in diffusion tensor imaging of neurodevelopment. NeuroImage 34 (1), 243–252.
Song, S., Yoshino, J., Le, T., Lin, S., Sun, S., Cross, A., Armstrong, R., 2005. Demyelination increases radial diffusivity in corpus callosum of mouse brain. NeuroImage 21, 132–140.
Song, S.-K., Sun, S.-W., Ju, W.-K., Lin, S.-J., Cross, A.H., Neufeld, A.H., 2003. Diffusion tensor imaging detects and differentiates axon and myelin degeneration in mouse optic nerve after retinal ischemia. NeuroImage 20 (3), 1714–1722.
Song, S.K., Sun, S.W., Ramsbottom, M.J., Chang, C., Russell, J., Cross, A.H., 2002. Dysmyelination revealed through MRI as increased radial (but unchanged axial) diffusion of water. NeuroImage 17 (3), 1429–1436.
Szeszko, P.R., Ardekani, B.A., Ashtari, M., Kumra, S., Robinson, D.G., Sevy, S., Gunduz-Bruce, H., Malhotra, A.K., Kane, J.M., Bilder, R.M., Lim, K.O., 2005. White matter abnormalities in first-episode schizophrenia or schizoaffective disorder: a diffusion tensor imaging study. Am. J. Psychiatry 162 (3), 602–605.
Van Hecke, W., Leemans, A., D'Agostino, E., De Backer, S., Vandervliet, E., Parizel, P.M., Sijbers, J., 2007. Nonrigid coregistration of diffusion tensor images using a viscous fluid model and mutual information. IEEE Trans. Med. Imaging. 26 (11), 1598–1612.
Van Hecke, W., Sijbers, J., D'Agostino, E., Maes, F., De Backer, S., Vandervliet, E., Parizel, P.M., Leemans, A., 2008. On the construction of an inter-subject diffusion tensor magnetic resonance atlas of the healthy human brain. NeuroImage 43 (1), 69–80.
Wang, F., Sun, Z., Du, X., Wang, X., Cong, Z., Zhang, H., Zhang, D., Hong, N., 2003. A diffusion tensor imaging study of middle and superior cerebellar peduncle in male patients with schizophrenia. Neurosci. Lett. 348 (3), 135–138.
Westerhausen, R., Walter, C., Kreuder, F., Wittling, R.A., Schweiger, E., Wittling, W., 2003. The influence of handedness and gender on the microstructure of the human corpus callosum: a diffusion-tensor magn reson imaging study. Neurosci. Lett. 351 (2), 99–102.
White, T., Kendi, A.T.K., Lehricy, S., Kendi, M., Karatekin, C., Guimaraes, A., Davenport, N., Schulz, S.C., Lim, K.O., 2007. Disruption of hippocampal connectivity in children and adolescents with schizophrenia – a voxel-based diffusion tensor imaging study. Schizophr. Res. 90 (1–3), 302–307.
Xie, S., Xiao, J.X., Gong, G.L., Zang, Y.F., Wang, Y.H., Wu, H.K., Jiang, X.X., 2006. Voxel-based detection of white matter abnormalities in mild Alzheimer disease. Neurology 66 (12), 1845–1849.
Xue, Z., Shen, D., Karacali, B., Stern, J., Rottenberg, D., Davatzikos, C., 2006. Simulating deformations of MR brain images for validation of atlas-based segmentation and registration algorithms. NeuroImage 33 (3), 855–866.
Yu, C.S., Zhu, C.Z., Li, K.C., Xuan, Y., Qin, W., Sun, H., Chan, P., 2007. Relapsing neuromyelitis optica and relapsing-remitting multiple sclerosis: differentiation at diffusion-tensor MR imaging of corpus callosum. Radiology 244 (1), 249–256.
Zhang, H., Avants, B.B., Yushkevich, P.A., Woo, J.H., Wang, S., McCluskey, L.F., Elman, L.B., Melhem, E.R., Gee, J.C., 2007. High-dimensional spatial normalization of diffusion tensor images improves the detection of white matter differences: an example study using amyotrophic lateral sclerosis. IEEE Trans. Med. Imaging. 26 (11), 1585–1597.